



HAL
open science

Optical Long Baseline Interferometry - Principles and Instrumentation

Denis Mourard, Nicolas Nardetto

► **To cite this version:**

Denis Mourard, Nicolas Nardetto. Optical Long Baseline Interferometry - Principles and Instrumentation. 2019. hal-03044567

HAL Id: hal-03044567

<https://hal.science/hal-03044567>

Submitted on 10 Dec 2020

HAL is a multi-disciplinary open access archive for the deposit and dissemination of scientific research documents, whether they are published or not. The documents may come from teaching and research institutions in France or abroad, or from public or private research centers.

L'archive ouverte pluridisciplinaire **HAL**, est destinée au dépôt et à la diffusion de documents scientifiques de niveau recherche, publiés ou non, émanant des établissements d'enseignement et de recherche français ou étrangers, des laboratoires publics ou privés.

Optical Long Baseline Interferometry

Principles and Instrumentation

Denis Mourard^{1,*} and *Nicolas Nardetto*¹

¹Université Côte d'Azur, OCA, CNRS, Lagrange, Parc Valrose, Bât. Fizeau, 06108 Nice cedex 02, France

Abstract. The principles of optical long baseline interferometry are presented firstly from the point of view of the coherence of the stellar wavefront and secondly from the point of view of the Object-Image relationship. These two complementary approaches permit to extract some important considerations for the actual implementation of this imaging technique. We also present a panorama of the currently operational optical interferometers and their most recent science programs. We conclude by a short prospective on the future steps.

1 Introduction

Researches in stellar physics have been, for a long time, dominated by well-established observational techniques like astrometry, photometry, polarimetry, and spectroscopy. But in all these techniques, except probably Doppler-imaging, the star is seen as a point-like source and the information on the spatial brightness distribution onto the sky is integrated. The star is considered as a source of light and the different properties of this light are sampled and analyzed. After the pioneering works at the beginning of the twentieth century by Michelson [1] and the original ideas by H. Fizeau [2], the rebirth of optical interferometry in 1974 by Antoine Labeyrie [3] has opened a completely new field of investigation: the high angular resolution permitting to reveal details at the surface or in the close environment of stars. As an imaging technique, optical interferometry requires a strict control of the quality of the optical transfer function and of the field of view. Moreover, the physical processes at work in stars dictate to combine the high spatial resolution with temporal or spectral resolution. Today, images of stellar's surface or detailed studies of the kinematic in atmospheres or disks are well established. Combined with the recent advent of exoplanet researches, and the instrumental progresses for asteroseismology or astrometry, stellar physics is clearly a central question among the top-priorities of today Astrophysics.

In this article, we will first present two complementary description of optical interferometry, either through the principles of coherence (Section 2) and those of imaging (Section 3). We then discuss, in Section 4, an important aspect of this observational technique that should be understood firstly as a direct imaging technique. Of course important practical limitations occur in reality, they will be presented in Section 5 and in Section 6. The paper will end with a panorama of the modern facilities in Section 7 and the most recent science programs in Section 8. We conclude by a few words on the future of this observational technique in Section 9.

*e-mail: denis.mourard@oca.eu

2 Angular diameter and coherence of the wavefront

Optical interferometry is often described through the concept of interference fringes. It was indeed the driving principles expressed by H. Fizeau [2]¹ and was described on the basis of the coherence of the wavefront. The excellent book of Goodman [4] is probably one of the reference work for optical interferometry. I'm presenting first this principle with a very simple demonstration.

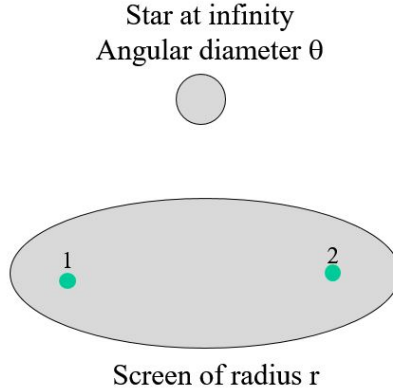


Figure 85. Schematic representation of an interferometer, from the point of view of the coherence of the wavefront.

In Fig. 85, I consider a star located at infinity and presenting an angular diameter θ . This object defines a solid angle Ω defined by:

$$\Omega = \pi \left(\frac{\theta}{2} \right)^2. \quad (195)$$

A screen of radius r and surface $S = \pi r^2$ intercepts the stellar wave. This defines a beam etendue ϵ that can be written as:

$$\epsilon = S \Omega = \pi^2 r^2 \left(\frac{\theta}{2} \right)^2. \quad (196)$$

The principle of coherence, as defined by Goodman in his book, indicates that we can consider the wave as coherent if $\epsilon < \lambda^2$. This defines the so-called radius of coherence r_c :

$$r_c = \frac{\lambda}{\pi \left(\frac{\theta}{2} \right)}. \quad (197)$$

One can note that in the case of a star with an angular diameter $\theta = 10mas$ and at a wavelength $\lambda = 1\mu m$, this leads to a value of $r_c \simeq 13m$. We thus understand that it exists a relation between the coherence of the wave and the angular diameter of the star. The coherence of the electromagnetic wave ψ could be determined by the computation of the complex degree of

¹Although the recognized reference for this discovery is dated from 1868, it exists a note of H. Fizeau at the French Academy of Sciences, dated from 1851, and showing that it could be possible to measure by interferometry, the apparent diameter of a source, and in particular of a star.

mutual coherence (Γ_{12}) between two points of the collecting screen separated by a distance B .

$$\Gamma_{12} = \frac{|\psi_1 \psi_2^*|}{\sqrt{|\psi_1|^2 |\psi_2|^2}}. \quad (198)$$

By using the Van-Cittert Zernike theorem and the notation \tilde{O} for the Fourier Transform of the star brightness distribution, we can write the following relation:

$$\Gamma_{12} = \frac{\tilde{O}(\frac{B}{\lambda})}{\tilde{O}(0)}. \quad (199)$$

Considering the star as a uniform disk, we finally obtain:

$$\Gamma_{12} = \left| \frac{2J_1(\pi B \theta / \lambda)}{\pi B \theta / \lambda} \right|. \quad (200)$$

The definition of coherence by Goodman corresponds to the case where $\Gamma_{12} = 0.5$ which corresponds to $\pi B \theta / \lambda = 2$ and thus to $B = r_c = \frac{\lambda}{\pi(\frac{\theta}{2})}$, which is an other way of defining the coherence ($\epsilon < \lambda^2$).

This simple calculation shows that the coherence of the electromagnetic wave of stellar sources could be measured through a spatial sampling if one can access to very long baselines (B larger than 100m typically). The simplest instrumental setup dedicated to the measurement of the complex degree of mutual coherence is thus to consider the coherent addition of the two complex waves collected at point 1 and 2 with a phase shift on the second one dedicated to the necessary adjustment of the optical path between the two wave collectors. Thus we obtain the total intensity I as:

$$I = |\psi_1 + \psi_2 e^{i\phi}|, \quad (201)$$

$$I = \psi_1^2 + \psi_2^2 + 2\psi_1 \psi_2 \times \cos(\phi). \quad (202)$$

Denoting I_i the intensity of the wave at point i , we finally obtain:

$$I = (I_1 + I_2) \left(1 + \frac{2\sqrt{I_1 I_2}}{I_1 + I_2} \times \frac{\psi_1 \psi_2^*}{\sqrt{|\psi_1|^2 |\psi_2|^2}} \times \cos(\phi) \right). \quad (203)$$

The term with the cosinus function represents, if one introduces variations of ϕ either by temporal or spatial sampling, a modulation in the measured intensity, which is also called interference fringes. The amplitude of the modulation is defined by the factor in front of the cosinus. It contains two parts: the photometric one ($\frac{2\sqrt{I_1 I_2}}{I_1 + I_2}$) and the coherence one ($\frac{\psi_1 \psi_2^*}{\sqrt{|\psi_1|^2 |\psi_2|^2}}$) where we recognize Γ_{12} the complex degree of mutual coherence of the two collected waves.

These principles are mainly valid whatever the wavelengths. But many other aspects have to be taken into account, such as the spectral and temporal coherence of the electromagnetic waves. Again at $\lambda = 1\mu m$, considering a spectral width $\Delta\lambda = 0.1\mu m$ leads to a coherence time $t_c = 3.10^{-14}s$ using the relation between the coherence time and the frequency domain ($t_c \times \Delta f = 1$). At larger wavelengths and with very fast detectors, it is possible to directly record the electromagnetic waves at two different locations and to correlate them, later, into a computer. This is usually done in radio-astronomy at millimeter and centimeter wavelengths

for Very Long Baseline Interferometry or, by reducing the spectral width and generating beating waves with a local oscillator, through what is called heterodyne interferometry. It could also be shown that the coherence of the electromagnetic wave could be extracted from the correlation between the fluctuation of intensities at the two different locations [5]. In this paper we only consider the case of direct interferometry in the optical domain, which means that we use detectors sensitive to the intensity of the electromagnetic wave recording the intensity resulting from the coherent addition of the complex waves.

As a conclusion of this section, we see that we have indeed a way to measure complex degrees of mutual coherence of stellar waves allowing us to sample the Fourier transform of brightness distributions at very high spatial frequencies. We will see in Section 6 how this method is now implemented in reality but before coming into the instrumental part of this technique an other point of view is also very important for a correct understanding of this observing technique.

3 Angular diameter and Object-Image relationship

Astronomers have developed optical interferometry in order to improve the resolving power of the telescopes. Indeed image formation in a telescope is a standard diffraction problem and it is known for a long time that an image $I(\vec{\alpha})$ is obtained as the convolution of the brightness distribution of the source $O(\vec{\alpha})$ by the point spread function of the optical device $H(\vec{\alpha})$.

$$I(\vec{\alpha}) = O(\vec{\alpha}) \otimes H(\vec{\alpha}) \quad (204)$$

When this convolution relation is translated into the Fourier domain, it shows that the spatial frequency spectrum of an image $\tilde{I}(\vec{u})$ is the spatial frequency spectrum of the object $\tilde{O}(\vec{u})$ filtered by the optical transfer function $\tilde{H}(\vec{u})$ of the optical device.

$$\tilde{I}(\vec{u}) = \tilde{O}(\vec{u}) \times \tilde{H}(\vec{u}) \quad (205)$$

Thanks to the diffraction principle, it could be easily shown (see the paper by J. Surdej in this book) that the modulus of the optical transfer function, called the modulation transfer function (MTF), is equal to the autocorrelation of the pupil function, defining the entrance plane of the optical device.

$$|\tilde{H}(\vec{u})| = AC [P(\lambda\vec{u})] \quad (206)$$

In the case of a monolithic telescope of diameter D , the MTF acts as a low pass filter transmitting the spatial frequencies of the object brightness distribution up to D/λ (see Fig. 86). This corresponds to what is usually called the diffraction limit λ/D of the telescope. We do not consider here the perturbations induced by the atmosphere and we just consider the ideal case of a perfect optical instrument.

In the case of an interferometer with two telescopes of diameter D and separated by a vector \vec{B} , the support of the MTF (also called the (u,v) plane), is made of a low frequency peak of extent $\pm D/\lambda$ and two high frequency peaks of extent $\pm D/\lambda$ and located at $\pm \vec{B}/\lambda$ (see Fig. 86). The interferometer acts thus as a high frequency band pass filter, allowing to reach information at a resolution of $\lambda/|\vec{B}|$.

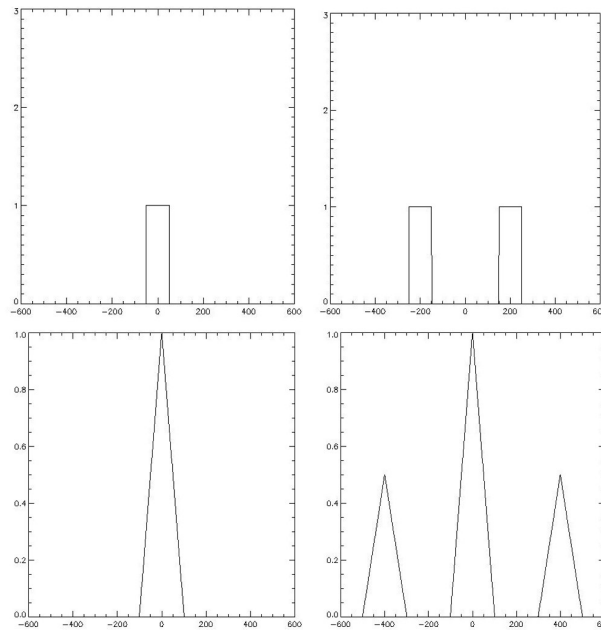


Figure 86. Modulation Transfer Function (bottom row) corresponding to the pupil (top row) of a single telescope (left) and of a 2-telescope interferometer (right). The units are arbitrary.

In the general case, the (u,v) plane (support of the MTF) is a function of the input baselines, of the latitude of the observatory, of the target coordinates, of the wavelength and of the time (because of the earth rotation). The (u,v) plane coverage defines the sampling of the Fourier transform of the object brightness distribution.

The properties of the image obtained directly at the focus of an interferometer clearly depend on the (u,v) plane coverage but it can also be shown [6] that the beam combination scheme plays also an important role in that domain. I refer the reader to the important papers published in that domain [7–10]. As an illustration I present in Fig. 87, some examples of (u,v) plane coverage and point spread function for different kind of optical interferometers.

Currently, no interferometer is working in a direct imaging scheme except the Large Binocular Telescope in its interferometric mode. The limitations of coherence for ground based projects in the optical domain are clearly difficult to overcome. Progresses are being made in that direction but for the moment, imaging at high angular resolution, is not working directly at the focus of the interferometer. Instead, astronomers are using the (u,v) plane coverage to sample the Fourier transform of the brightness distribution and then to reconstruct images. This method has made great progresses in the recent years. The quality of the reconstructed images highly depends of the (u,v) plane coverage and of the *a priori* information (regularization constraints) introduced in the reconstruction algorithm. I do not intend to describe this method in the present paper and I refer the reader to the practical sessions of the school.

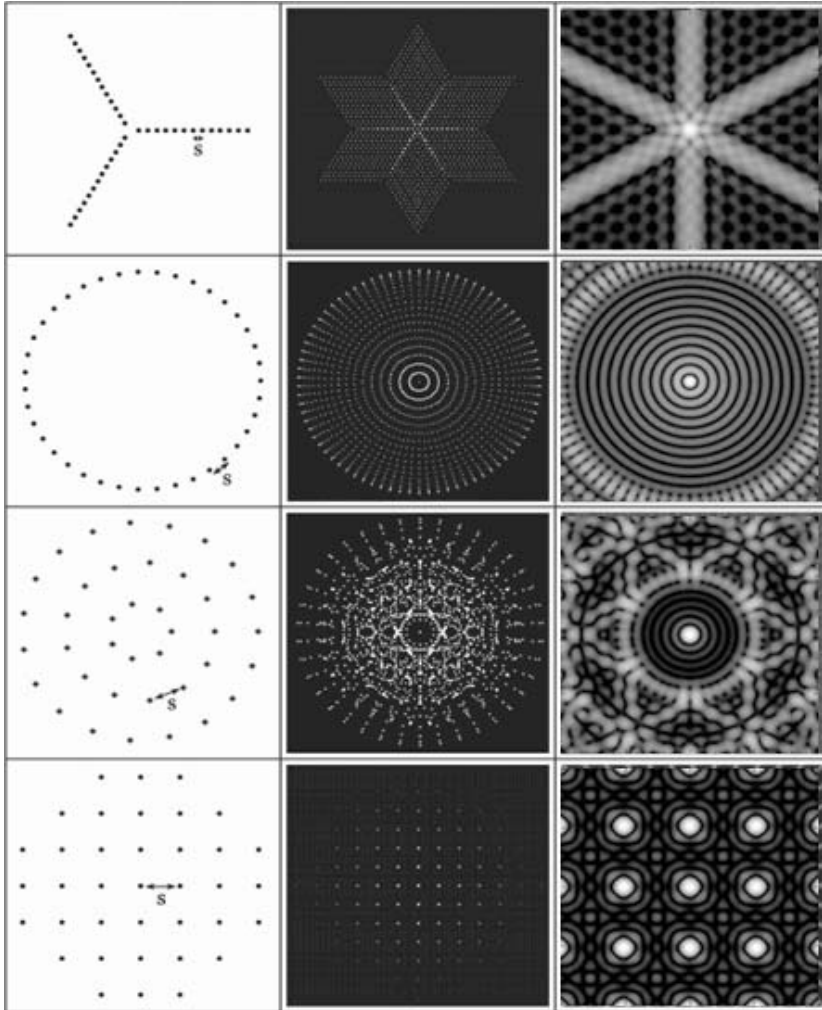


Figure 87. Examples of (u,v) plane coverage (middle column, autocorrelation of the pupil) and of the corresponding point spread function (right column, modulus of the Fourier transform of the autocorrelation of the pupil) for four different input pupil (left column) configurations.

I will conclude this section by giving some general considerations about image reconstruction with an interferometer. First of all, an interferometer made of N telescopes produces $N(N - 1)/2$ baselines and thus samples $N(N - 1)/2$ frequencies in the Fourier transform of the brightness distribution of the object. We thus have a problem with $N(N - 1)/2$ complex unknowns.

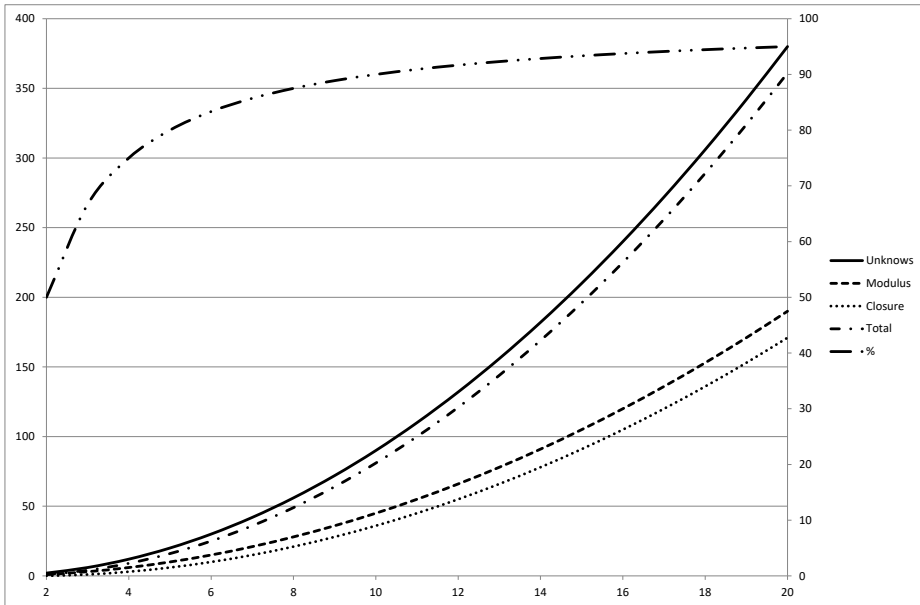


Figure 88. Number of unknowns, of modulus and closure phase measurements (left scale) as a function of the number of telescopes. The dark curve represents the percentage (right scale) of information measured as a function of the number of telescopes.

We have already indicated that the limitations of ground based interferometers are dominated by the phase effects introduced by the atmospheric turbulence. If it is easy to measure the modulus of the Fourier transform over the $N(N-1)/2$ points, the phase measurements are however highly corrupted by the turbulence. As in radio interferometry, astronomers overcome this difficulty by computing closure phase measurements over triplets of apertures. It can be shown easily that the atmospheric phase terms are removed in the sum of the phase of three interference fringes over any triplet of telescopes. Thus closure phase measurements (see explanations in Section 6) give us access to $(N-1)(N-2)/2$ additional measurements. With this in hand, we understand that the problem is not well constrained because the number of unknowns is always larger than the number of measurements. A representation of these numbers is presented on Fig. 88.

4 A direct imaging technique

We concluded the previous section on the idea that, ideally, an interferometer may have the same imaging properties as a single giant telescope. If this is true from the point of view of the optical system, in practice the encoding of the information is quite different and to reach this ultimate goal the implementation of interferometers should respect a certain number of conditions and some restrictions appear. A schematic representation of two generic configurations of interferometers is given in Fig. 89. The first case (A) represents what is usually

called the Fizeau combination. The two segments are really identical to elements of the giant parabola and if the number of sub-elements is increased the imaging properties of the diluted parabola approach the ones of the giant mirror. The transfer function is not as rich as for the full pupil but the main property of the highest angular resolution could be easily preserved.

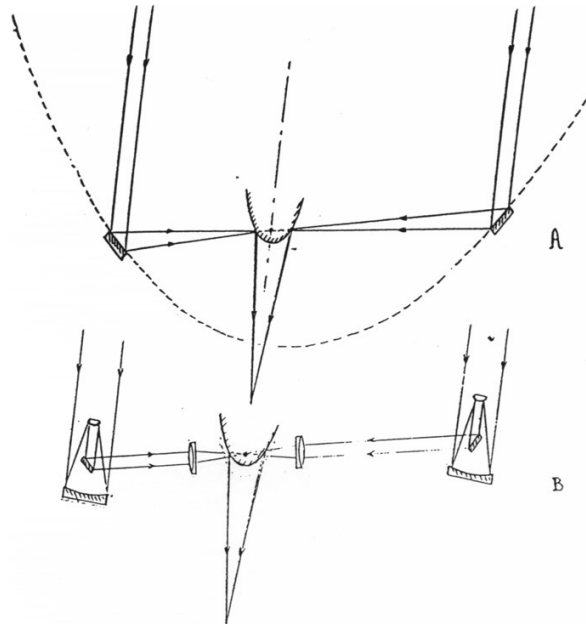


Figure 89. Schematic representation of an interferometer. A: the Fizeau type, B: the Michelson type.

This figure helps us to understand that the same formalism of image formation is in action when considering an interferometer and not only of single telescope. This property of convolution has been studied with many details by Labeyrie [6] and by Tallon&Tallon-Bosc [11]. These works have generated the idea that an interferometer could work as a direct imager and not only as an aperture-synthesis experiment sampling the spatial frequency plane and allowing an, *a posteriori*, image reconstruction. A direct image could be obtained at the common focus of the interferometric array. This was known in the Fizeau-like mode but this one is not efficient as the sampling is far from being optimized. The pupil-densification scheme and the hypertelescope principle have permitted to develop a new way of thinking the interferometers, just as direct-imaging devices. In Fig. 90, I present the Fizeau Point Spread Function for different pupil configurations. If we can easily understand that with an increasing number of sub pupils, the point spread function is progressively converging towards the point spread function of the large monolithic telescope, we also identified that the interferometric Fizeau process generates also a large number of bright side peaks in the point spread function, degrading therefore the image quality. This poor imaging quality can be overcome by using the principle of pupil densification as this is done implicitly in fact in almost all aperture synthesis interferometers, and even in the Michelson experiment presented in Fig. 91. Thanks to this important aspect of the beam combination in an interferometer, it is possible to have a fixed sampling of fringes whatever the entrance pupil. The pupil densification adds an important constraint with respect to the standard pupil reconfiguration of current interferometers: the geometry of the input and output pupil has to be respected but each output pupil could be magnified to improve the direct imaging properties. Of course there is a price to pay because

the convolution relation is broken in this densification process. The drawback is a reduction of the field of view but it can be shown that in the direct imaging field, a pseudo relation of convolution exists and that a true direct image is indeed formed. The properties of this direct imaging scheme (Clean Field, Direct Imaging Field, Interferometric Field, encircled energy) have been studied in many details by different authors [7, 8]. I present in Fig.92 various possible interferometric arrays and in Fig. 93 their imaging properties in a densified combination scheme.

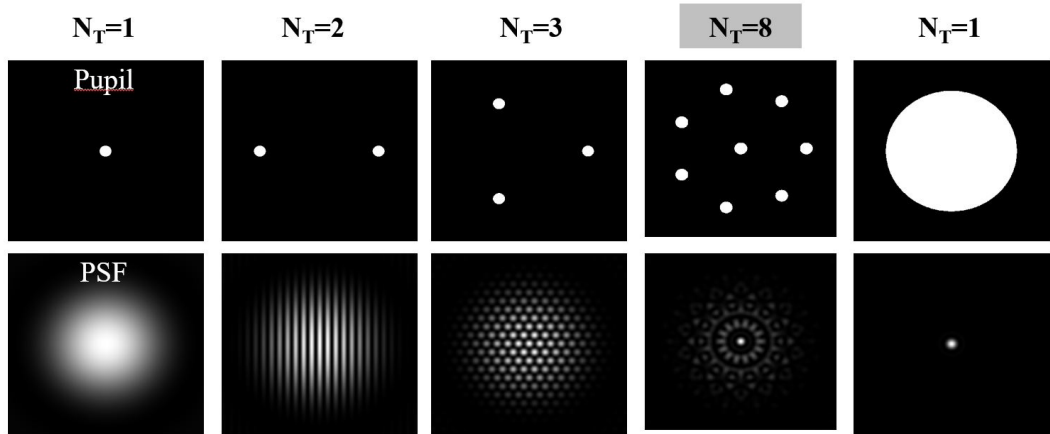


Figure 90. The upper row presents different pupils, from a small telescope to a large telescope, and with three different interferometric pupils. The bottom row presents the corresponding point spread function.

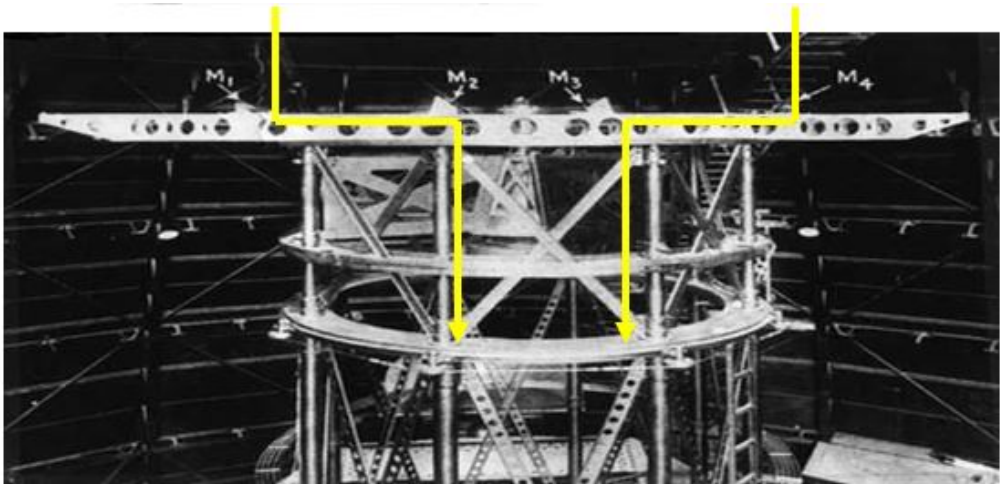


Figure 91. The Michelson interferometer mounted on top of the Hooker 100 inches telescope at Mount Wilson. The light path used 2 flat mirrors in each arm, generating an apparent pupil, as seen from the eyepiece, always the same, independently of the distance of the two entrance mirrors. This fixed output pupil generates a fixed fringe spacing and realizes in fact the first densification.

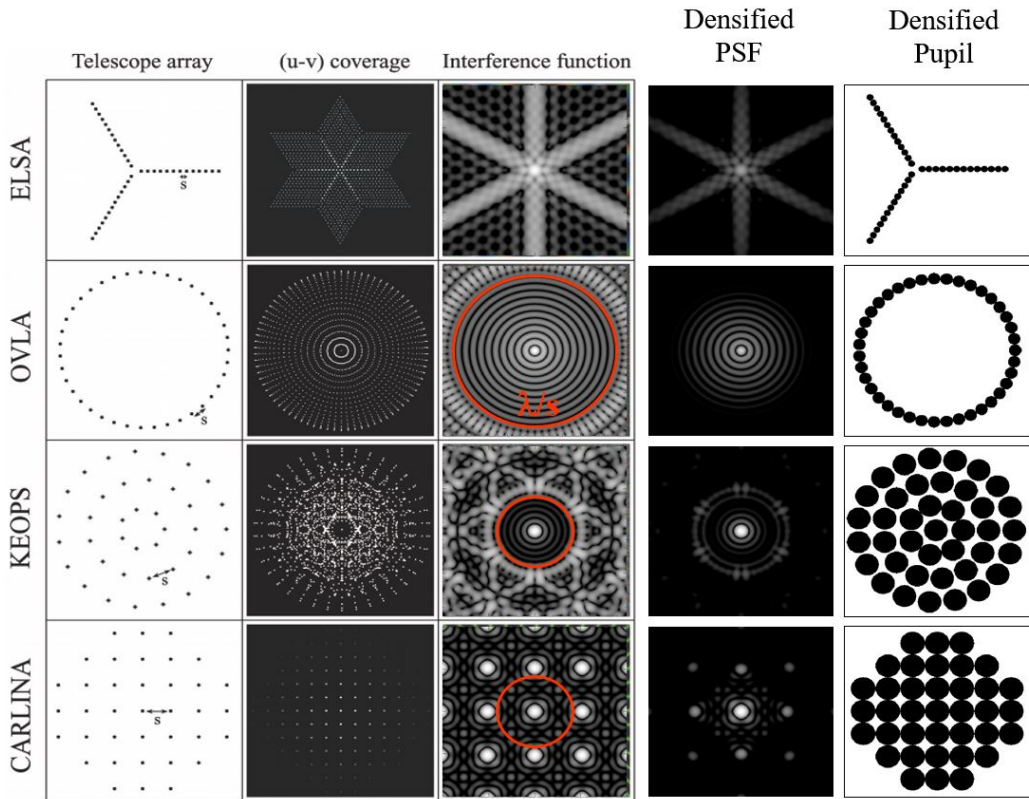


Figure 92. Four different possible interferometric arrays with their respective (u,v) plane coverage, the representation of the interference function, the densified point spread function, and the corresponding densified pupil.

In this section, I have presented the principle of optical interferometry from the direct imaging point of view. With the limitation in the field of view generated by the beam combination and the violation of the strict convolution product in the image-object relationship, we can however consider that an hypertelescope is not different from any imaging telescope. But we must also recognize that it has taken a very long time to obtain images with interferometers and the hypertelescope principle is, today, still in its demonstration phase. The largest part of the astrophysical publications in optical interferometry continue to work with squared visibility, closure phase, triple product amplitude, and model reconstruction or parametric imaging. The main reason behind the current limitations is again a problem of coherence and its strong limitation because of the atmospheric turbulence and the actual implementation of long baseline interferometers. This is also a budgetary issue but we will not cover this aspect of the problem in the present paper.

5 The reality of the coherence

If we look again at Eq. 197 in Sec. 2, defining the radius of coherence r_c , we can easily deduce that for a star with an apparent angular diameter of 10 mas , at a wavelength of $1 \mu\text{m}$, the radius of coherence is of the order of 13 m. Considering a spectral bandwidth of $0.1 \mu\text{m}$,

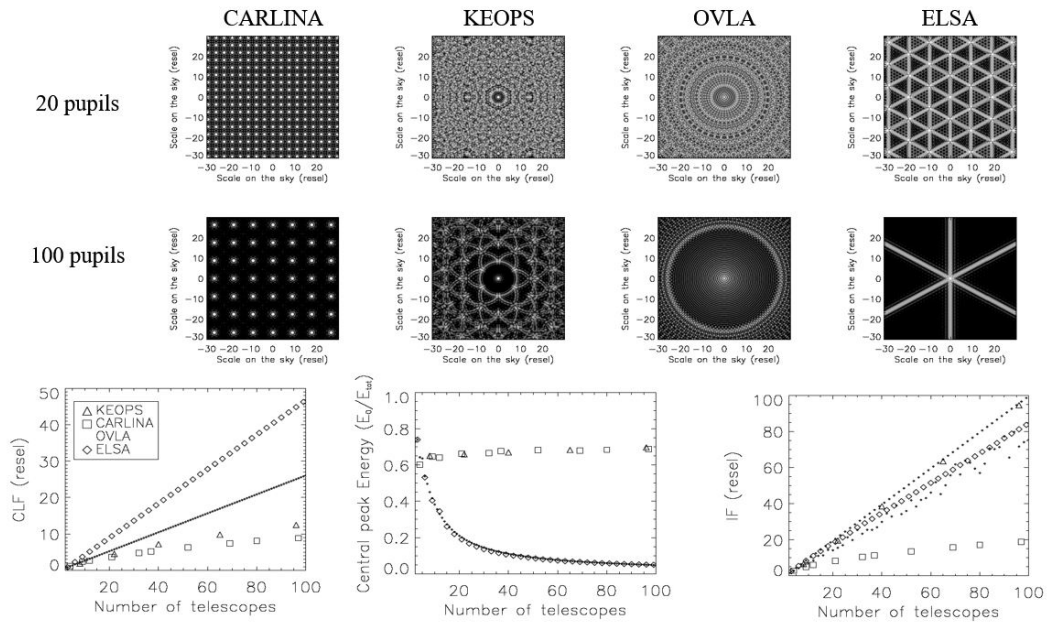


Figure 93. The four interferometric arrays are considered with a variable number of subpupils and the imaging properties are compared, in terms of Clean Field, of encircled energy, and of interferometric field of view.

this corresponds to a coherence duration of 3×10^{-14} s and finally a coherence length of $10 \mu\text{m}$. It means that, independently of any other consideration, the optical paths between the different arms of the interferometer should be equalized at a level of a fraction of the coherence length if one wants to be able to detect the interferometric pattern and to measure it with good quality. For obvious reasons of correlation, the interferometric signal (the fringe contrast) depends on the residual error on the optical path and if this error is not stable the transfer function of the interferometer is degraded.

Interferometers have been equipped with different kinds of delay lines to compensate for the earth rotation and to guaranty the equalization of the optical paths. The usual setup of such delay lines is a mechanical carriage moving on rails thanks to a motorized wheel. The optical system, usually a cat's eye, is supported by a second carriage, whose position could be corrected precisely with a second level of control loop over a small stroke of one millimeter or less, usually made of a voice-coil. It permits to compensate the defaults of the main driving system. And finally the secondary mirror of the cat's eye is usually supported by a piezo translation stage able to correct the optical path at a very high frequency (a few kiloHertz) over a very small stroke.

The combination of these three control loops permits strokes of a few tens of meters with a precision less than 10 nanometers for speeds up to 10mm/s. An example is presented in Fig. 94. Today the technology of delay lines is very mature and the performance is excellent, even at the shortest wavelengths.

There is however a second important difficulty in terms of coherence of the stellar wavefronts due to the atmospheric turbulence. The gradients of temperature and speed inside the turbulent medium generate important variations of the index of refraction of air. When the turbulence is developed, a statistical description of the residual coherence is usually made.



Figure 94. One of the VLTI delay line installed on its rails and supporting the cat's eye.

Astronomical sites are of course carefully studied in terms of seeing properties in complement with overall weather and transparency characteristics. The spatial coherence of the atmosphere is usually described by the Fried parameter r_0 , of the order of 10 cm in good sites. The temporal coherence is designed by the coherence time τ_0 , of the order of 10ms. Finally, at least at visible wavelength, there is an additional characteristic that has to be taken into account which is called the spectral coherence of the atmosphere, of the order of 30 nm in the R band. This quantity corresponds to the decorrelation of the speckles and fringes between two distant spectral bands [12]. All these parameters are usually correlated, even if one can find sites with large r_0 and small τ_0 but we consider that the hypervolume of coherence (the one that is directly related to the quality of the interferometric measurement) varies as the power 4 of the turbulence (two spatial dimensions, one temporal, and one spectral). Moreover, the spatial and temporal coherence (r_0 and τ_0) vary as $\lambda^{6/5}$ which also explains why near and mid infrared interferometry has been preferred for a long time, in addition of course to the simple consideration related to the size of the wavelength.

To avoid the effects of the atmospheric turbulence, one obvious solution is to implement interferometers in space. This has been pushed a lot twenty years ago, especially for the science case of the direct characterization of earth-like planets (TPF, Darwin) but the cost of these missions and, on certain aspects, the technological maturity have killed the efforts. Moreover, the maturity of the ground interferometers was also not well established at that time. Finally, today, the situation of space interferometers is not encouraging at all and no clear path forward could be established.

The progress of technology and of fast control loops on ground systems (see the paper by F. Martinache in this book) have permitted to develop cophasing devices permitting to compensate the negative aspects of the atmospheric turbulence. The individual telescopes could be equipped with adaptive optics (usually simple one based on the principle of Single Conjugated Adaptive Optics for a very narrow field). Coherencing devices have been developed

for a long time [13] in order to stabilize the optical path difference within a small fraction of the coherence length. More recently, and after the pioneering work of FINITO [14] on the VLTI, cophasing devices permitting to stabilize the optical path difference within a fraction of the wavelength, have been successfully implemented within the GRAVITY instrument on the VLTI [15].

So, the coherence of the stellar wavefront could be measured with the current interferometers implemented on ground if different levels of active and adaptive compensation are implemented: delay lines for the compensation of the earth rotation, adaptive optics on each individual telescope to correctly use the full collecting area, and finally a cophasing device to correct for the difference of piston between the different arms of the interferometers. With the effective implementation of all these active systems, the different samples of the incoming stellar flat wavefront are fully recophased and the ultimate performance could be reached, almost like in a classical giant telescope with a diluted pupil.

6 Practical considerations for the implementation of an interferometer

Looking back now to the schematic representation of the two types of interferometers (see Fig. 89), it is clearly understandable that the Fizeau configuration (A) is not easy to implement on ground (because of the need for a giant driving system) and the classical way of doing interferometers on ground is the second scheme (case B), usually called the Michelson configuration. In this case the two segments of the giant parabola are replaced by independent telescopes and the light is recombined at the common focus.

We should focus first our attention on one general geometric particularity of this system. The entrance pupil plane is now made of independent subpupils that are separated by tens or hundreds of meter. Therefore the quality of the optical transfer function will highly depend on the control of the sub pupils, in terms of transverse and longitudinal position. Moreover the global pupil plane is no longer perpendicular to the direction of pointing, as it was the case in the Fizeau configuration or for any standard telescope. Optical delay appears between the two arms and delay lines are mandatory. An important atmospheric dispersion may appear because of the prism of air above the pupil, and finally the subpupils are at variable distance from the focus which may generate Fresnel diffraction [16]. The first conclusion is that a complex optical system is needed between the collection of the wavefronts and the interferometric focus (see Fig. 95).

Now that the beams are correctly transported to the common interferometric focus we should optically form the interferometric signal described in Eq. 201 of Sec. 2. Two options could be considered: a coaxial beam combiner with a temporal modulation (see left panel of Fig. 96) or a multi-axial combiner with a spatial modulation (right panel of Fig. 96). The first mode is well adapted to single pixel detectors and was, therefore, used for a long time at the beginning of infrared interferometry. The low noise and large number of pixels of the detectors in the visible have permitted to prefer the second scheme in the visible. The recent progresses of infrared detectors have progressively reduced the interest of the co-axial combination.

With these schemes of combination, the interferometric equation (Eq. 203 of Sec. 2) is formed with a dependence of the term ϕ in the cosine function, either with time (co-axial scheme) or position (multi-axial scheme).

Pending the actual implementation of direct imaging interferometers, the current instruments are based on the measurements of the fringe properties, mainly contrast and phase. The first measurement is the contrast C of the fringes which is usually defined as:

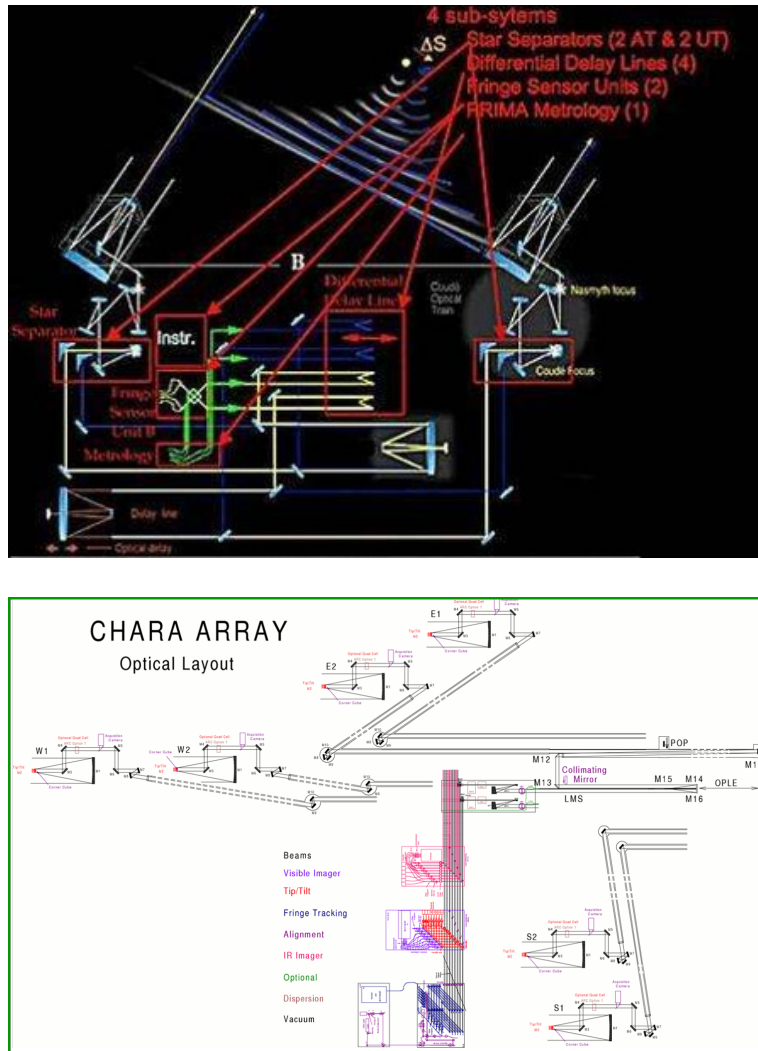


Figure 95. The complex optical Coude train of the VLTI (top) and CHARA (bottom) interferometers.

$$C = \frac{I_{max} - I_{min}}{I_{max} + I_{min}}. \quad (207)$$

With the simplifying hypothesis $I_2 = I_1$ meaning that no photometric difference exists in the two beams, we can easily deduce that the contrast is an estimation of the complex degree of mutual coherence, also called the squared visibility V^2 .

$$C = V^2 = \frac{|\psi_1 \psi_2^*|}{\sqrt{|\psi_1|^2 |\psi_2|^2}}. \quad (208)$$

It can be shown also that extracting the squared visibility could be done by the so-called ABCD technique. The principle is to measure the intensity of the signal over four phase

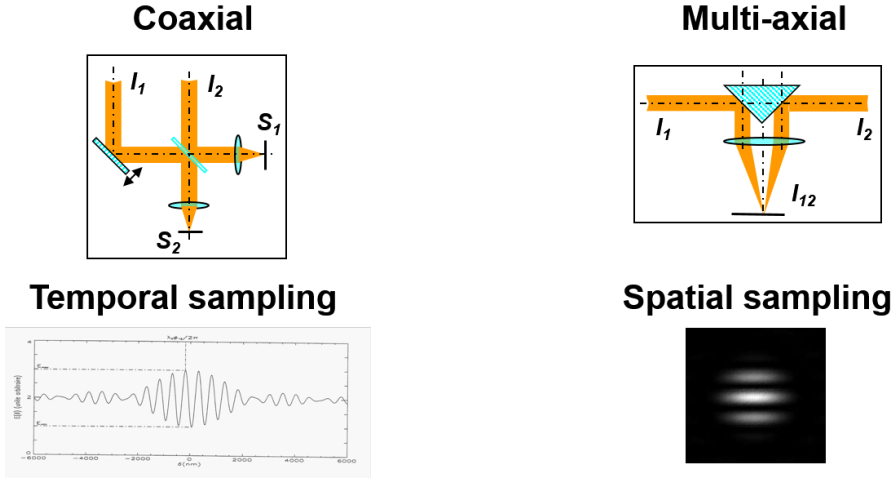


Figure 96. The two generic beam combiners for optical interferometry: (left) co-axial and temporal modulation, (right) multi-axial and spatial modulation. The bottom row gives a representation of the fringe signal, as a function of time (left) or as a function of the position on the detector (right).

intervals covering: $A = [0; \pi/2]$, $B = [\pi/2; \pi]$, $C = [\pi, 3\pi/2]$, and $D = [3\pi/2, 2\pi]$. The contrast is obtained with the following formula:

$$C = V^2 = \frac{\pi}{\sqrt{2}} \frac{\sqrt{(I_A - I_C)^2 + (I_B - I_D)^2}}{I_A + I_B + I_C + I_D} \quad (209)$$

The ABCD technique is more usually used for measuring the phase of the fringes on a very efficient way and the first technique with I_{min} and I_{max} is not easily implementable because of the fast motion of the fringes due to the atmospheric turbulence. Mathematically speaking, these two techniques are in fact equivalent, from a numerical point of view, to discrete Fourier transform of the fringe equation. And this is in fact the usual way to measure the fringe contrast, through a Fourier transform of the raw images.

The measurement of the phase of the fringes is usually more complicated because of the atmospheric turbulence. Differential measurements between two different spectral bands are possible and permit to get rid of the atmospheric phase. This has been used a lot and it is usually estimated through the argument of the cross-spectrum:

$$Arg(\langle \tilde{I}_{\lambda_1} \tilde{I}_{\lambda_2}^* \rangle) = Arg(\tilde{O}_{\lambda_1}(\frac{B}{\lambda})) - Arg(\tilde{O}_{\lambda_2}(\frac{B}{\lambda})). \quad (210)$$

Another possibility, inspired from what has been developed for a long time in radio-astronomy [17], is the so-called closure phase, as mentioned in Section 3 and Fig. 4. One has to consider a triplet of telescopes as in Fig. 6:

The phases (ψ_{12} , ψ_{23} , and ψ_{31}) of the fringes over the different baselines could be expressed as following:

$$\begin{aligned} \psi_{12} &= \Phi_{12} + \varphi_1 - \varphi_2 \\ \psi_{23} &= \Phi_{23} + \varphi_2 - \varphi_3 \\ \psi_{31} &= \Phi_{31} + \varphi_3 - \varphi_1 \end{aligned}$$

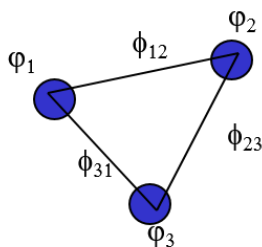


Figure 97. A triplet of telescopes used for measuring closure phase. The atmospheric phases on each telescope are indicated (φ_1 , φ_2 , and φ_3). Over the three baselines (12-23-31), the phases (Φ_{12} , Φ_{23} , and Φ_{31}) of the Fourier Transform of the object brightness distribution are also indicated.

Getting rid of the atmospheric phase is possible by forming the following expression called the closure phase:

$$\text{ClosurePhase} = \psi_{12} + \psi_{23} + \psi_{31} = \Phi_{12} + \Phi_{23} + \Phi_{31}. \quad (211)$$

Summing the phase of the three fringes system on a closed triplet of telescopes permits to obtain an information on the phase of the Object without the perturbation of the atmospheric phase.

With the squared visibility, the differential phase and differential visibility, and the closure phase, we have now a complete description of the interferometric observables. We have seen at the end of Sect. 3, and in particular, in Fig. 88, how many of these quantities are accessible for an interferometer with a number N of telescopes. In the next Section, I will present a short overview of the existing facilities and of their main science drivers.

7 A modern panorama of optical long baseline interferometry

After a few decades of development, modern optical interferometry is now focused on four facilities: ESO/VLTI, CHARA, NPOI, and MROI.

7.1 NPOI

NPOI² is a collaboration between US Naval Observatory (USNO), Naval Research Lab (NRL), and Lowell Observatory. NPOI has a long story and was part of the pioneering installations at the end of the previous century. The major part of its program is dedicated to global precision astrometry for the maintenance of the coordinates and proper motion of reference stars. But NPOI has also obtained very impressive results in stellar physics, on single stars or multiple systems. It is equipped with a Classic combiner based on a temporally modulating combiner and avalanche photodiodes. It covers the visible domain (550 to 850 nm) with a resolution of 40 and offers 16 independent spectral channels. NPOI has a sensitivity limit of $m_V \approx 5.5$ with the 6+4 (imaging+astrometric) siderostats, 12 cm in diameter, equipping the array. Recently a new EMCCD-based spatially modulating combiner called VISION has been developed [18]. It can accommodate up to 6 beams and offers two spectral resolutions (200 and 1000) in the visible domain. NPOI is currently being upgraded with larger telescopes (1 m in diameter) and the infrastructure for enabling the 450 m baselines of the Anderson Mesa site.

²<http://www2.lowell.edu/rsch/npoi/index.php>

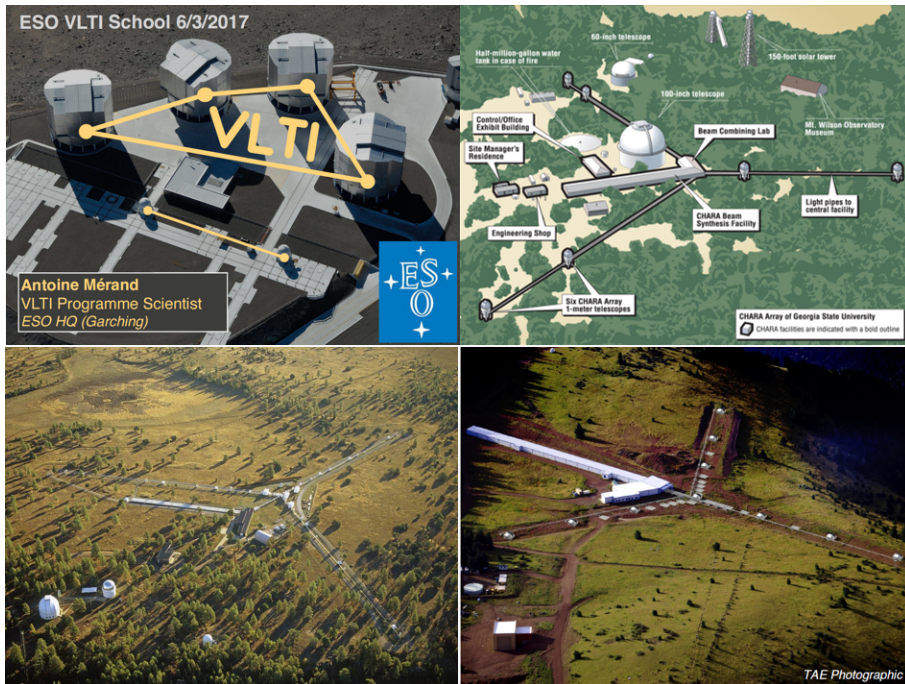


Figure 98. A panorama of the four optical interferometers existing today in the world. We recognize the Very Large Telescope Interferometer or VLTI (upper-left panel) installed at Cerro Paranal on the premises of ESO. The Center for High Angular Resolution in Astronomy or CHARA Array, developed by the Georgia State University (upper-right panel) is installed on Mount Wilson, California. In the bottom row, the Navy Precision Optical Interferometer (NPOI) is located on Mesa Anderson, close to Flagstaff - Arizona (bottom-left panel). And finally the Magdalena Ridge Optical Interferometer (MROI) is today in construction phase on the site of the Magdalena Ridge Observatory - New Mexico (bottom-right panel).

7.2 MROI

The MROI³ is in construction phase. The baseline plan is to equip the Array in Y-shape with ten 1.4m telescopes with the possibility of relocation on baselines between 8 and 350m. It is designed for imaging the central zone of active galactic nuclei, the study of the star and planet formation, and the physical processes of stellar accretion and mass loss. The first telescope has been delivered on site during Spring 2018 and many developments are still ongoing like innovative evacuated delay lines or a fringe tracker for phase stabilization. The implementation of the full facility is however funding dependent.

7.3 The VLTI array

The ESO/VLTI Array⁴ is installed on the ESO premises at Cerro Paranal in Chile. The four 8.2-m Unit Telescopes (UTs) and the four 1.8-m Auxiliary Telescopes (ATs) are the light collecting elements of the VLTI. The UTs are set on fixed locations while the ATs can be

³<http://www.mro.nmt.edu/about-mro/interferometer-mroi/>

⁴<https://www.eso.org/sci/facilities/paranal/telescopes/vlti.html>

relocated on 30 different stations. After the light beams have passed through a complex system of mirrors and the light paths have been equalized by the delay line system, the light re-combination is performed for quadruplet of telescopes with the beam combiners PIONIER, GRAVITY, and MATISSE. The first generation instruments (VINCI, MIDI, AMBER) are now decommissioned. Due to its characteristics, the VLTI has become a very attractive means for scientific research on various objects like young pre-main sequence stars and their protoplanetary disks, post-main sequence mass-losing stars, binary objects and their orbits, solar system asteroids, our galactic center, and extragalactic objects such as active galactic nuclei.

PIONIER [19] is a H-band 4-beam combiner instrument. It was originally a visitor instrument that by agreement with IPAG is offered to the ESO community from P96 onwards as a facility instrument, i.e. without the need for collaborating with the instrument team, and is offered both in visitor and service mode for normal, large, and monitoring programs. PIONIER combines either beams from the 8.2-m Unit Telescopes or from the 1.8-m Auxiliary Telescopes to provide visibilities of six different baselines, as well as four closure phase measurements, simultaneously. PIONIER features low resolution spectroscopic optics to measure at six different wavelengths within the H-band, increasing the (u,v) coverage, or can work in integrated light for sensitivity enhancement on faint targets.

GRAVITY [15] is an interferometric instrument operating in the K band, between 2.0 and 2.4 μm . It combines 4 telescope beams and is designed to perform both interferometric imaging and astrometry by phase referencing. The instrument delivers spectrally dispersed interferometric quantities in low, medium, and high spectral resolution. GRAVITY's angular resolution is set by the maximum separation of the employed telescopes and the field of view of the instrument. In imaging mode, GRAVITY is able to resolve features between 4 mas (milli-arcsecond) and 50 mas with the UTs, and between 2 mas and 140 mas with the ATs. The astrometric accuracy is also given by the maximum separation of the telescopes and will be of the order of few 10 to 100 μas . GRAVITY is equipped with a dedicated fringe tracking subsystem and with a dedicated IR wavefront sensing system (CIAO) on the UTs.

MATISSE [20] is a mid-infrared spectro-interferometer combining the beams of up to 4 UTs/ATs. The instrument sensitivity, sampling and throughput are optimized for L and N. The L band is specified from 3.2 to 3.9 μm and the N band from 8.0 to 13.0 μm . MATISSE will operate also in M band, from 4.5 to 5.0 μm . The L, M and N bands can be observed simultaneously. The instrument will be able to observe with different spectral resolutions. Two spectral resolutions are possible in N band ($R \approx 30$, $R \approx 200$) and 3 in L&M bands ($R \approx 30$, $R \approx 500$ for L and M, $R \approx 1000$ for L only). Due to readout time, the full simultaneous coverage of the L&M bands in low and medium resolutions, and the full coverage of the L band in high spectral resolution require an external fringe tracker. MATISSE will measure: coherent flux, visibilities, closure phases and differential phases. Differential visibilities can also be derived. These quantities will be measured as a function of the wavelength in the selected spectral bands and resolutions. The objective of MATISSE is image reconstruction. It will extend the astrophysical potential of the VLTI by overcoming the ambiguities existing in the interpretation of simple visibility measurements.

7.4 The CHARA array

The Center for High Angular Resolution Astronomy (CHARA⁵) optical interferometric array of six telescopes is located on Mount Wilson, California. Each telescope of the CHARA Array has a light-collecting mirror 1-meter in diameter. The telescopes are dispersed over

⁵<http://www.chara.gsu.edu/>

the mountain to provide a two-dimensional layout that provides the resolving capability of a single telescope with a diameter of 330 meters. Light from the individual telescopes is transported through vacuum tubes to a central Beam Synthesis Facility in which the six beams are combined together. When the paths of the individual beams are matched to an accuracy of less than one micron, after the light traverses distances of hundreds of meters, the Array then acts like a single coherent telescope for the purposes of achieving exceptionally high angular resolution. The Array is capable of resolving details as small as 200 micro-arcseconds. The strength of the CHARA Array besides in the number and size of its individual telescopes, its ability to operate at visible and near infrared wavelengths, and its longest baselines of 330 meters.

The CLASSIC and CLIMB beam combiners [21] of the CHARA Array are open air, aperture plane, broadband, single spectral channel instruments optimized for sensitivity. CLASSIC is the original two beam combiner used for the first science at CHARA, and it still has the faintest magnitude limit. CLIMB is a three beam expansion of CLASSIC that also provides closure phase measurements. It is a very useful coherence tracker for the visible combiners.

JouFLU [22] is a two telescope beam combiner operating in the near infrared K band ($\lambda = 2.20\mu\text{m}$). JouFLU spatially filters the light through optical fibers to produce high precision visibility measurements.

The Michigan Infrared Combiner (MIRC [23]) combines the light from all six CHARA telescopes simultaneously. It disperses the light across 8 spectral channels in the near infrared H-band ($1.6\mu\text{m}$). MIRC can be used to create images of stellar surfaces. The precision closure phases are well suited to detecting faint binary companions.

PAVO [24] is an integral-field-unit for measuring spatially-modulated fringes in the pupil plane. It spectrally disperses light over a 630-950 nm bandwidth ($R = 30$). Currently, PAVO can be used to combine the light from two telescopes.

The Visible spEctroGraph and polArimeter (VEGA [25, 26]) was installed in September 2007 at the CHARA array. VEGA measures spectrally dispersed interference fringes, providing a spatial resolution of 0.3 mas and spectral resolutions from $R = 6,000$ to 30,000 over a wavelength of 480-850nm. It can combine 2, 3, or 4 telescopes.

8 The study of stellar surface and their close environment using interferometry

In this section we will present some of the most exciting results obtained using interferometry in the recent years. We will focus on stellar physics, i.e. the study of stellar surface and their close environment, following the framework of the 2017 edition of the Evry Schatzman school of the French national program of stellar Physics (PNPS). One can see in Fig. 99 that the number of refereed publications using interferometry (considering all topics) has grown continuously to a maximum in 2009, and remains a very active domain of research. The new generation of instruments that are just arriving now will probably continue this growth.

As we will show, interferometric, direct and Doppler imaging are very complementary approaches, while the synergy between interferometry and asteroseismology is powerful in the context of *Gaia* and PLATO space missions.

8.1 Imaging at very high angular resolution

Four centuries after Giordano Bruno, one of the dreams in astronomy is to make the image of an exo-Earth located at say 10 light years to find traces of life. However, to achieve this objective, it would be necessary, for example, to build a 150 km space hypertelescope (see

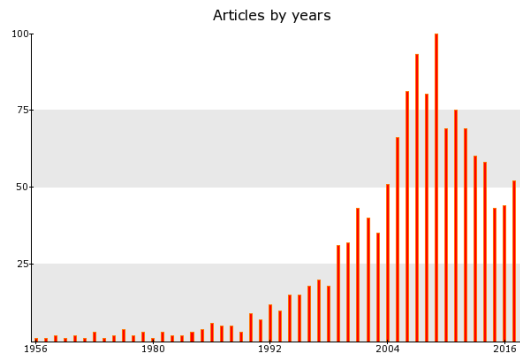


Figure 99. Histogram of refereed publications in interferometry (considering all topics). *Source: statistics done by the Jean-Marie Mariotti Center (JMMC, <http://apps.jmmc.fr/bibdb/>).*

Fig. 100). This example shows the difficulty of the task, with both problems of angular resolution and contrast. Thus, what can be done first, and is in fact absolutely necessary to understand the planet, is to image the stars and in particular, the most resolved stars, such as giant stars or red supergiants.



Figure 100. Simulated image of the planet Earth located 10 light-years away and observed by a 150 km hypertelescope consisting of a network of 150 3m mirrors in the visible domain [27].

8.1.1 Giant and red supergiants stars

We can for instance cite the interferometric image of the red giant π^1 Gruis (radius of $350 R_{\odot}$), obtained by the PIONIER instrument at VLTI, which reveals for the first time granulation patterns on the surface of a star [28] (see Fig. 101). Valuable information on the geometry and dynamics of the granulation is obtained from interferometric observations, even if the coverage of the spatial frequency plane is insufficient to produce an image. Several studies have been conducted, first on the red supergiant Betelgeuse [29], then Antares [30] and finally on the red giant β Oph with the instrument MIRC on the interferometer CHARA [31]. Let's also mention a series of remarkable images obtained on a giant, ζ And, with the instrument MIRC on CHARA [32] (see Fig. 102) which made it possible to detect a dark spot during a cycle of rotation of the star. Note that these observations of red giants or supergiants stars generally require a heavy investment in terms of numerical computation time in order to produce a 3-dimensional model of the star [33] to interpret the visibility and phase closure measurements.

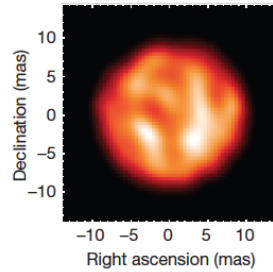


Figure 101. The surface of the red giant π^1 Gruis imaged by the PIONIER instrument on the VLT [28], i.e. with a hectometric base and in K band.

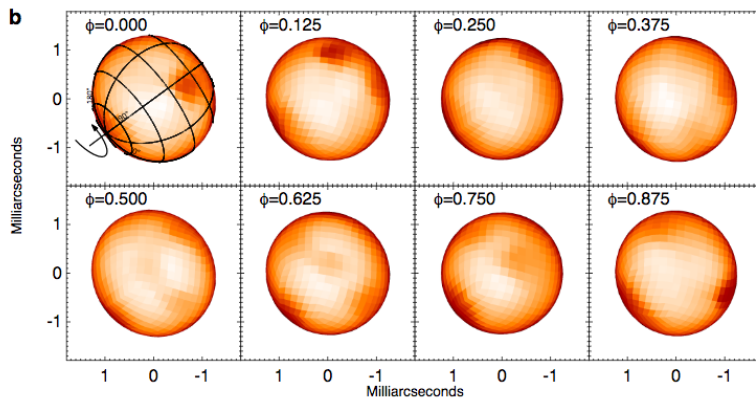


Figure 102. The surface of the giant ζ And obtained with the instrument MIRC on CHARA [32]. We can see a persistent spot at the pole of the star and a transient spot moving with the rotation of the star.

To go further in the analysis of this type of astrophysical objects, it becomes interesting to adopt precisely a multi-technique or multi-wavelength strategy. We will give two examples here.

- First, it should be noted that a strong linear polarization was detected in the Betelgeuse [34] atomic lines, in several other red supergiants [35], as well as in Mira or RV Tau pulsating stars [36]. This polarization in the spectral lines makes it possible to go back to the geometry of a possible bright spot on the disk of the star, a spot that can also be detected by interferometry. Thus, the bright spots observed on the interferometric images of Betelgeuse [29] have also been detected by spectro-polarimetry [34]. Thus, a remarkable synergy between interferometric and Doppler imaging appears. And it may be noted in this regard that the VEGA instrument on the CHARA interferometer has a polarimetric mode, thus allowing spectro-polaro-interferometry, but this mode is not used on a regular basis [37].
- Another example is given by a multi-wavelength AGB L2 Pup approach, observed in the visible with the ZIMPOL/SPHERE instrument of the VLT [38] on the one hand, and with the radio interferometer ALMA [39] on the other hand. What is remarkable here is that the angular resolution of a telescope of 8 meters in the visible (16 mas) is almost identical to

that obtained by the kilometer bases of ALMA in the radio domain at 0.9 mm (14 mas). It thus becomes possible to superimpose two images at identical angular resolutions, but at two different wavelengths. While SPHERE gives indications on the geometry of the observed object, ALMA provides, because of its spectral resolution, constraints on the kinematics of the environment in the CO line (see Fig. 103). It is interesting to mention that we will obtain in the future the same type of synergy, i.e. images of equivalent angular resolution, between ZIMPOL/VLT in the visible and a K-band ELT, or between an ELT in the visible and MATISSE/VLTI in N-band (Fig. 104).

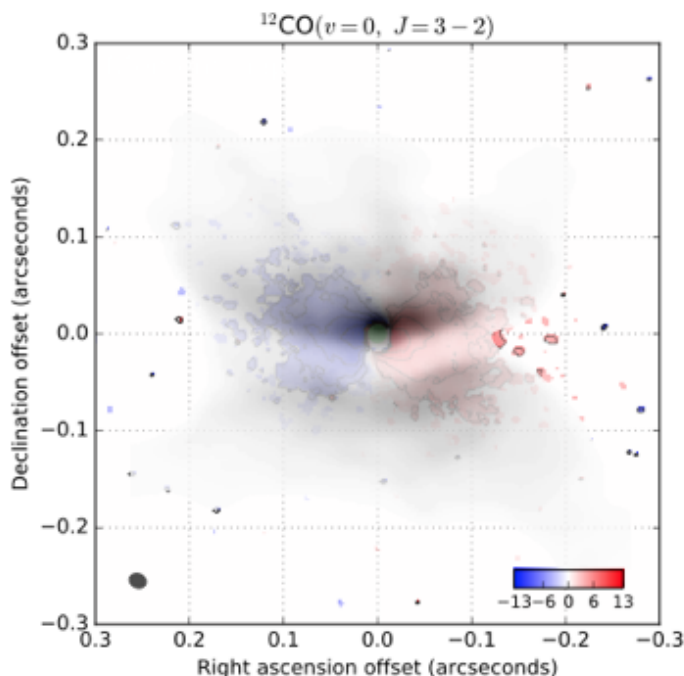


Figure 103. Superimposition of L2 Pup images obtained with ZIMPOL/SPHERE [38] and ALMA [39]. The image in gray color corresponds to the observations of ZIMPOL/SPHERE instrument on the VLTI. In color (blue / red) appears the velocity fields (in km.s^{-1}) as measured by ALMA. These two images have the same angular resolution, which perfectly illustrates the potential of a multi-wavelength approach.

Giant and supergiant imaging is thus a very dynamic field of research. But, failing to be able to image the exoplanets, another synergy appears around the *detection* of the exoplanets by imagery.

8.1.2 The star/planet interaction

The high angular resolution is a powerful tool that currently allows, especially with the SPHERE instrument on the VLT to detect exoplanets by imaging. An interesting example concerns the GJ504 system [40]. As the subtitle of this publication "*Combining interferometric, radial velocity, and high contrast imaging data*" indicates, this is a good example of synergy between IRDIS/SPHERE observations on the VLT which allow to detect the exoplanet,

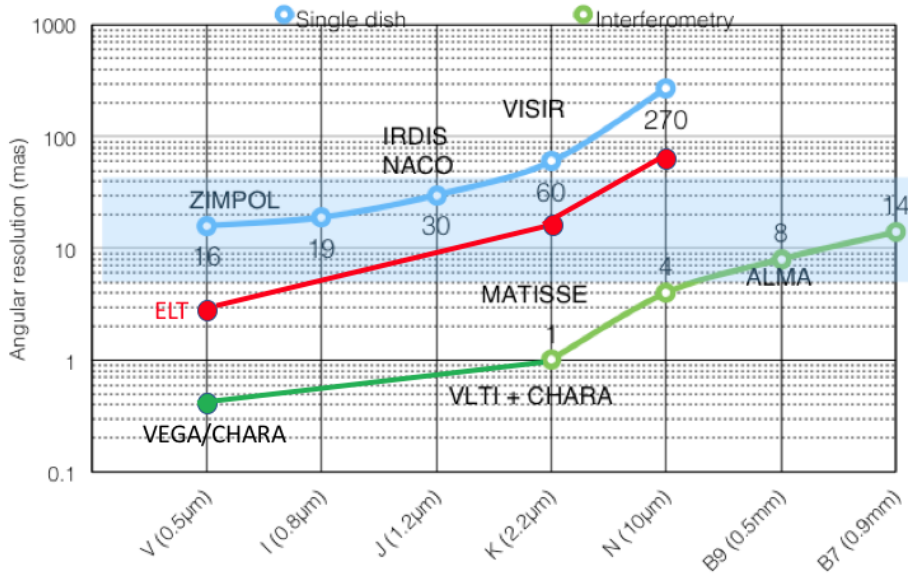


Figure 104. Comparison of the angular resolution of monolithic telescopes and existing interferometric arrays as a function of wavelength. It is thus possible to obtain images of equivalent angular resolution with ZIMPOL/SPHERE on the VLT in the visible and the interferometric ALMA interferometric array in the B9 band at 0.9 mm (see Fig. 103). In the same way, we can anticipate interesting future synergies between the ELT in the K band, ZIMPOL and ALMA (B9); or between the visible ELT and the MATISSE interferometric instrument on the N-band VLTI.

and interferometric observations VEGA/CHARA [41], which, in turn, make it possible to constrain the angular diameter of the central star. This angular diameter, combined with a measurement of parallax provides the radius of the star, which in turn provide strong constraints on the age of the system, a crucial information to better characterize the fundamental parameters of the star-planet pair.

8.1.3 The rotating stars

Fast rotators are generally smaller angularly, and therefore more difficult to image than the giant or supergiant stars, but significant efforts have been made in recent years in this field of research. We can mention for instance the image of the star Achernar, the closest and brightest rotating star of the sky, obtained with the instrument PIONIER on the VLTI. The 'e' indicates that there is a Balmer emission line due to the circumstellar environment of the star, which appears and disappears periodically. Achernar's 2014 images show an excess of continuous emission in the H band with a spatial extension of typically 2 stellar radii [42] (see Fig. 105).

The study of Be's disks is also an active field of research and we can present here the remarkable results obtained on ϕ Per with the complementary contribution of the MIRC and VEGA instruments on CHARA. The MIRC instrument (in H band, with a resolution 4 times lower than in the visible range with VEGA) made it possible to image the disc of the star, as well as the orbit of the companion (Fig. 106). The VEGA data, with the combination of the spatial and spectral resolution of the instrument, provide images of the disk of the star

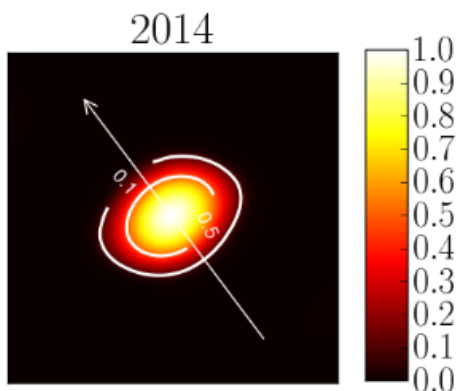


Figure 105. Pionier/VLTI image of Archenar secured in 2014. The arrow corresponds to the axis of rotation of the star whose equatorial angular diameter is close to 2 mas [42]

at different wavelengths in the hydrogen line $H\alpha$, which gives access to the disc kinematics [43]. This example shows the need of combining interferometric instruments at different wavelengths, and, as such, the availability of the different instruments within CHARA is particularly profitable for many projects in stellar physics. This also applies to the VLTI, and even between the VLTI and CHARA for some objects close to the ecliptic.

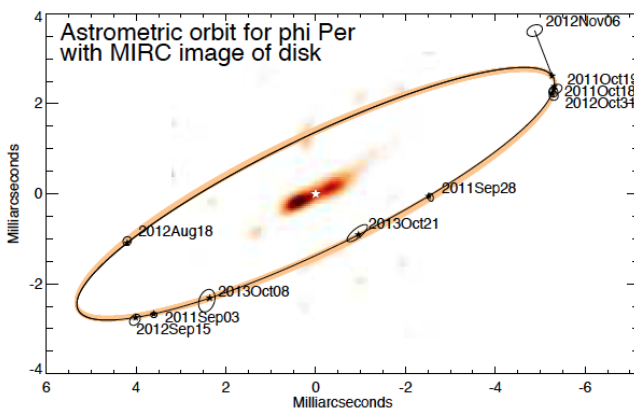


Figure 106. On this image obtained with the instrument MIRC on CHARA, we see the disc of the Be star ϕ Per (the star itself has been removed) as well as the orbit of the companion.

In addition to the environment (disk) of Be-type stars, the surface of rapidly rotating stars is also interesting to study, since it exhibits a flattening effect, as well as a gravitational darkening due to a gradient of temperature and gravity. Interferometry is a technique adapted to the study of these geometric properties. Visibility and closure phase measurements are indeed used to constrain the parameters of the model of the rotating star. For instance, the CHARRON code was recently used to analyze the PIONIER data of Archenar [44]. Beside, it should be mentioned that the gravitational darkening is particularly well contrasted in the visible range, and that the first measurements in this wavelength domain although incomplete

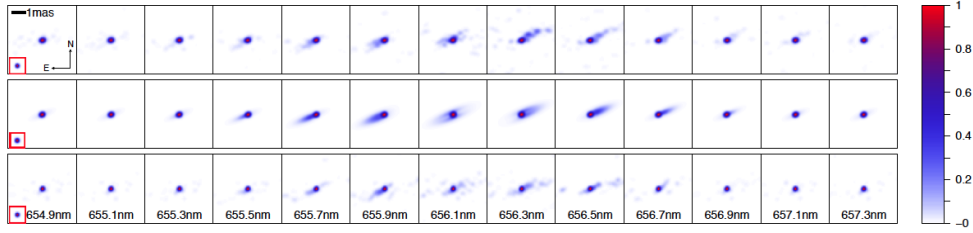


Figure 107. The polychromatic images of ϕ Per in the $H\alpha$ line, a good tracer of the kinematics of the rotating disc) obtained by the VEGA / CHARA instrument (at the top) are compared to a model (medium), itself artificially degraded by a model of the instrument (below). This figure is taken from [43].

(without phase closure) remain valuable. Thus, [45] measured a flattening of 12% for δ Per in the visible domain, and deduced a speed of rotation of 57% of the critical speed (i.e. maximum speed allowed for the stability of the star).

8.2 Cepheids and eclipsing binaries as distance indicators in the universe

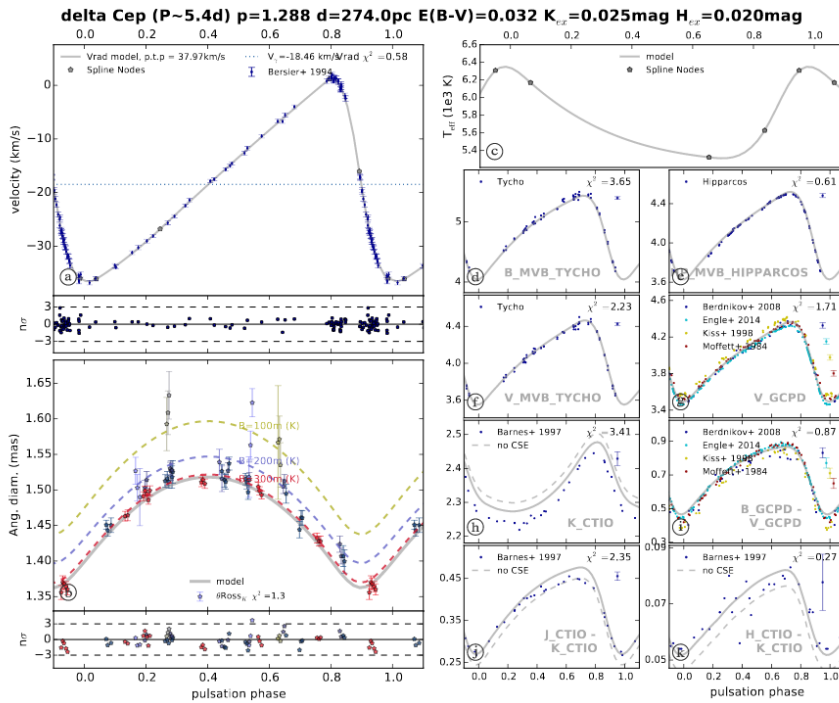


Figure 108. SpectroPhoto-Interferometry of Pulsating Stars (SPIPS) is a version of the Baade-Wesselink distance determination method that combines observations of different types (photometry, velocimetry and interferometry) to constrain the parameters of a quasi-static model of pulsation of the Cepheid (here δ Cep), and in particular its distance [46].

Interferometry plays a key role in the calibration of distance scales in the universe, and this at different levels. Indeed, to understand the nature of dark energy, we must measure the rate of expansion of the universe, that is to say the Hubble constant (H_0), with a good precision, i.e. better than 2%. The two main methods for doing this, the study of the cosmic background radiation and the determination of distances in the universe show significant disagreements, which we refer to as the 'tension'. One of the ways to solve this tension is to better calibrate the period-luminosity relation (PL) of Cepheids: what is its zero point? Is it sensitive to metallicity? Can we reduce the dispersion of the relationship? The method based on eclipsing binaries has recently been used to reach the 2.2% precision on the LMC distance [47], which makes it possible to constrain the zero point of the PL relation and to study the effect of metallicity. The eclipsing binary method is based on a very simple concept: the linear radii of the two components of the eclipsing binary are deduced from photometric and spectroscopic observations, while the corresponding angular diameters are calculated from a surface brightness-color relationships, which is precisely calibrated by interferometry. As part of the international project Araucaria⁶, the current goal is to reach 1% on the accuracy on these relations [48, 49], especially for KIII-type giant stars (such as those found in LMC eclipsing binaries). This will allow to reach the 1% precision on the distance of LMC. Similar efforts aim to calibrate the surface-brightness color relationships for early types stars (O, A, B) [45], that we find in M31 and M33 eclipsing binaries, two key galaxies for the calibration of the PL relationship.

Moreover, applying the Baade-Wesselink method (see the recent SPIPS version, Fig. 108) of distance determination to the Cepheids of the Magellanic clouds is now possible [50], but the projection factor and its dependence with the Cepheid pulsation period remains a key-issue, except perhaps for δ Cep, a well-understood prototypical star [51]. It is therefore crucial to refine our understanding of the atmospheric dynamics of Cepheids and their environment to determine distances in the universe. This is particularly true as the envelopes of the Cepheids could have an non-universal effect on the dispersion of the period-luminosity relation. Cepheid envelopes were detected by infrared interferometry [52], but rather surprisingly, an envelope around δ Cep was recently detected in the visible range by the VEGA/CHARA interferometer contributing to 7% of the flux of the star [53]. An effort is currently done to understand the structure and the physico-chemical nature of these envelopes, as well as their distribution in the instability strip.

8.3 Young stellar objects

Finally, we will discuss the contribution of imagery and high angular resolution to the study of young stars. These objects are complex with most of the time a circumstellar disc, whose material is accreted toward the central star, then ejected and collimated into a jet. We thus try to understand the geometrical structure of the disc, its physico-chemical nature, as well as the links with the planetary formation. For these young stellar objects the multi-wavelength approach is particularly suitable: the outer part of the disk is probed by radio interferometry, with ALMA for example (see the section on young objects), the medium-infrared allows to determine the molecular composition of the heart of the disc (soon with MATISSE / VLTI), while the near infrared (K band) and the ionized gas (Br γ , AMBER/VLTI line) allow to probe the inner edge of the dust disc. Concerning the visible domain, it allows us to get even closer to the star (ionized gas probed by the line H α with VEGA/CHARA), while the UV emission informs us about the magneto-spheric accretion and energy processes related to the jet. Here are some examples:

⁶<https://araucaria.camk.edu.pl/>

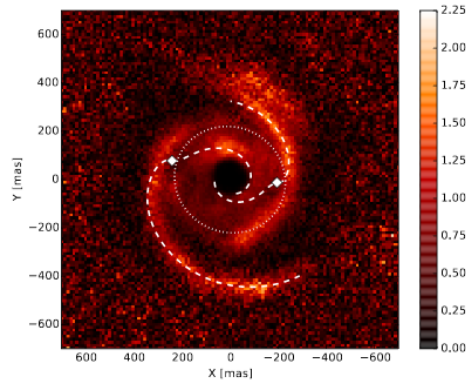


Figure 109. Polarized light image of the SPHERE/VLT protoplanetary disk MWC758 in the infrared. The two diamonds correspond to planets. The dotted ellipse corresponds to a projected circle with a radius of 250 mas [54].

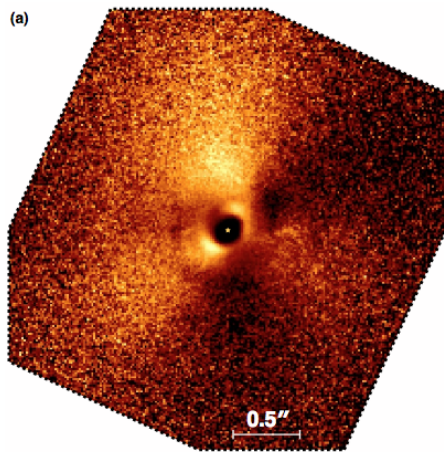


Figure 110. HD100546 observations of ZIMPOL/SPHERE in polarized light with a resolution for this object of 2 au. Structures in the discs are clearly detected and can be understood as an interaction between the disk and planets [55].

- First, let us take the example of VEGA data on CHARA obtained in different spectral channels of the $H\alpha$ emitting line of the Herbig Ae/Be star AB Aur [57], which is an excellent tracer of the geometry and kinematics of the ionized gas just below the inner edge of the disk of dust (0.05 - 0.15 au), and which indeed showed that there was an accretion wind on the innermost part of the disk.
- Then, let's continue our way out with [58] that probed the inner part of the HD50138 disk, a pre- or post-primary B[e] star using AMBER/VLTI observations in the $B\gamma$ line. These observations show that the zone of emission of the ionized hydrogen gas is closer to the star (< 3 au) than the emission due to the dust continuum, which helps to constrain the geometry of the object. These observations also show that the disk has a Keplerian rotation.

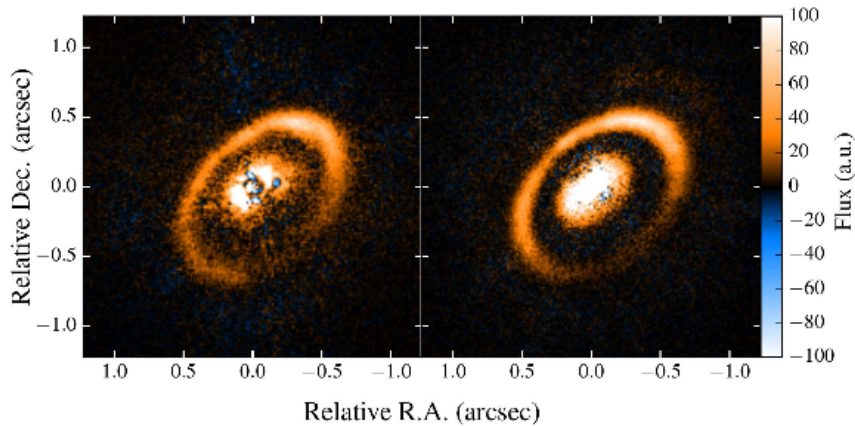


Figure 111. Left, observations ZIMPOL/SPHERE of HD163296 in polarized light, and corresponding model on the right (see [56] for more details).

- Recently, thanks to its sensitivity, the GRAVITY instrument of the VLTI [59] has been able to probe the emission Br γ at scales lower than the astronomical unit. [60] observed S CrA, a double classical T Tauri star located at a distance of 130 pc. The continuum (K band) allows to resolve two disks of radius 0.1 ua each, having a tilt and a very similar position angle, which suggests that they stem from the fragmentation of a single disk. The visibility signature as a function of the wavelength makes it possible to detect and locate spatially the emissions of the He I and Br γ lines, showing an inverse P Cygni profile, characteristic of an accreting gas. The Br γ emission is compact with a radius of ~ 0.06 ua, about twice as large as the truncation radius of the inner disk, and traces mainly a wind. In the coming years other observations of a sample of T Tauri stars with different masses, ages and disk properties are planned with GRAVITY.
- This type of statistical approach is already underway with the PIONIER/VLTI observation of 21 T Tauri type stars. [61] have shown that for 13 of them there is a disc, whose scattered light (in band H) extends beyond 3 ua (at 150 pc). Each object looks different and an analysis job is in progress.
- Finally, on a larger scale, many results have been obtained by SPHERE/VLT. First, [54] unveiled an extremely complex structure within the MWC 758 protoplanetary disk between 26ua and 148ua, using observations in infrared polarized light. These SPHERE/VLT observations confirm the presence of two spirals, whose origin is attributed to two planets (see Fig. 109). Let us also mention the results obtained with SPHERE on the protoplanetary disk LkCa15 [62], as well as the results obtained by [55] on HD100546 (see Fig. 110), or HD163296 [56] (see Fig. 109) and HD169142 [41].
- Concerning the external parts of the protoplanetary disks, which are mainly probed by ALMA, we refer the reader to the following publications (**to be specified**).

8.4 The prototypic star β Lyrae

In this short section, we would like to show a recent result [63] concerning the interacting binary β Lyrae which perfectly illustrates the relevance of a global approach on a prototypical

object. β Lyrae is an extremely complex object studied since 1830 and which has made the subject of more than 850 publications. The combination of a rich bibliographic heritage, new photometric and interferometric data (NPOI, CHARA/MIRC and VEGA) associated with a complex model (SHELLPEC) allowed to provide a coherent understanding of the object, whose figure 112 gives a representation. The coordination of photometric, spectroscopic and interferometric observations has permitted a global modeling from UV to far IR. The structure of the accreting disk, its temperature profile demonstrate that it is not in hydrostatic equilibrium. A mass transfer is thus clearly established. Authors have also demonstrated that a hot spot appears on the disk and that it is clearly related to the mass transfer from the donor.

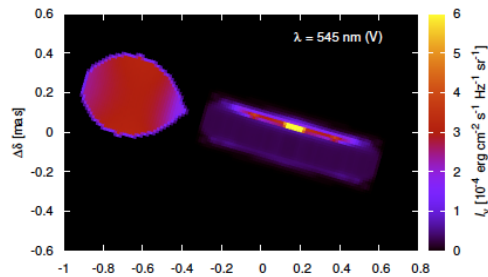


Figure 112. Three-dimensional model of β Lyrae (SHELLPEC), constrained by photometric and interferometric data NPOI, MIRC and VEGA on CHARA [63]

So far we have been interested in 'stellar zoology' in high angular resolution, i.e. in their activity (granulation, rotation, pulsation) or their environment (Be and/or protoplanetary disks, envelope of AGB or Cepheids). We will now enter another field, that is the fundamental parameters of stars and planets.

8.5 Interferometry, asteroseismology and fundamental stellar and planetary parameters

The Figure 113 (*shorty R. Ligi*), illustrates the path and synergy between interferometry, asteroseismology and the precise and exact determination of stellar and planetary parameters.

Let's start at the top of the figure. Interferometry requires surface-brightness color relationships (or equivalent) to determine the angular diameter of its calibrators, and hence, to calibrate the visibility measurements corresponding to the star to be studied⁷. A remarkable work has been to provide a catalog (the JSDC: 'The Stellar JMMC Diameter Catalog' version 2) which contains the estimated angular diameter for 465877 stars, with a median error of 1.5 % and possible bias of the order of 2% [64]. Nevertheless, it must be kept in mind that the activity of the star (wind, environment, spots, granulation, rotation) has an effect on the estimate of the diameter of the calibrator and/or the star science⁸. The rapid rotation has for example an effect on the estimate of the diameter of stars O, A, B of the order of a few percent [45, 65].

It should also be noted that the conversion between the "uniform" angular diameter θ_{UD} and "darkened" θ_{LD} , i.e. taking into account the limb-darkening of the star requires a model of the atmosphere of the star. Efforts are currently done to quantify the effect of a 1D or 3D

⁷These are precisely the same relationships that are used to determine the distance of eclipsing binaries, see section above

⁸It should be kept in mind that the accuracy on the diameter of the interferometric calibrator is not linearly related to the accuracy on the diameter of the star science

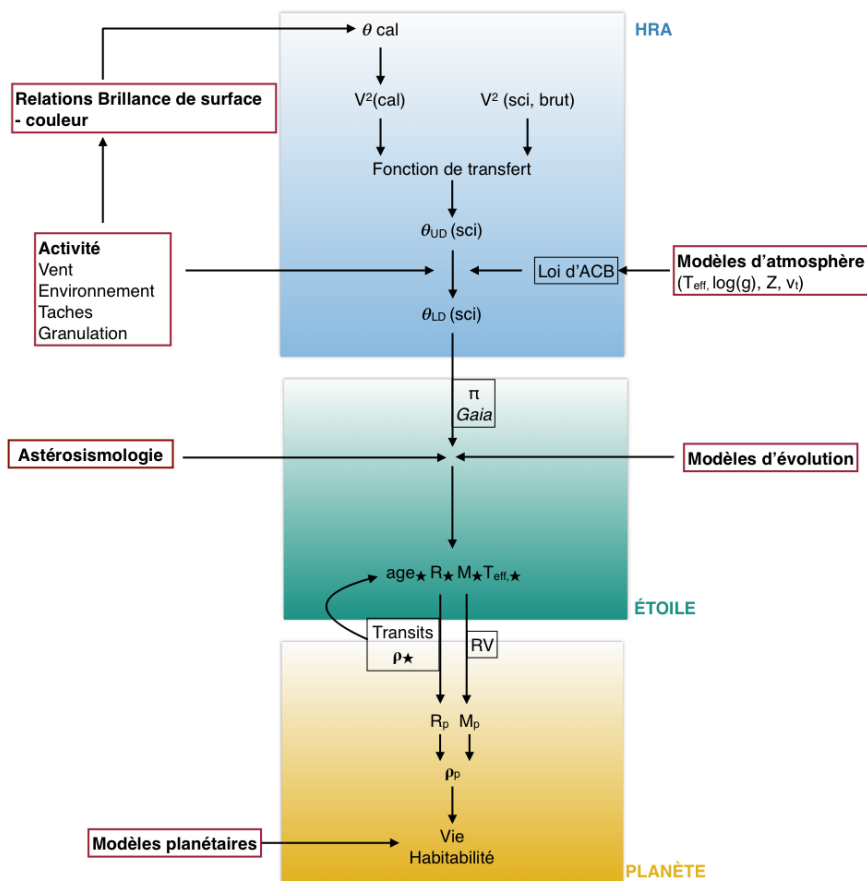


Figure 113. Interferometry, asteroseismology and fundamental stellar and planetary parameters. This figure illustrates how interferometric angular diameters, combined with precise and accurate parallax measurements (*Gaia*), constrain asteroseismic models, which in turn (*via* current and future planetary transient measurements with PLATO) allow to deduce the radius of the planet from the radius of the star.

model on the interferometric estimation of the angular diameter, especially for the giant [66–68]. This work is particularly interesting as it is now possible, for only a few stars, to measure *directly* the limb-darkening of a star by interferometry. Limb-darkening is therefore not assumed (based on a 1D or 3D atmosphere model), but directly measured using precise and accurate visibility measurements at high spatial frequencies. Note at this level the remarkable result obtained on α Cen A & B with the PIONIER instrument on the VLTI [69], which made it possible to measure the limb-darkening of the star. These measurements indicate lower limb-darkening than the values predicted by the 1D or 3D models (see Fig. 114).

Once the angular diameter of the star is determined independently by interferometry, it is then possible to combine it with a measure of *Gaia* parallax (for example) to deduce the radius of the star and then compare it with a radius estimate from asteroseismic measure-

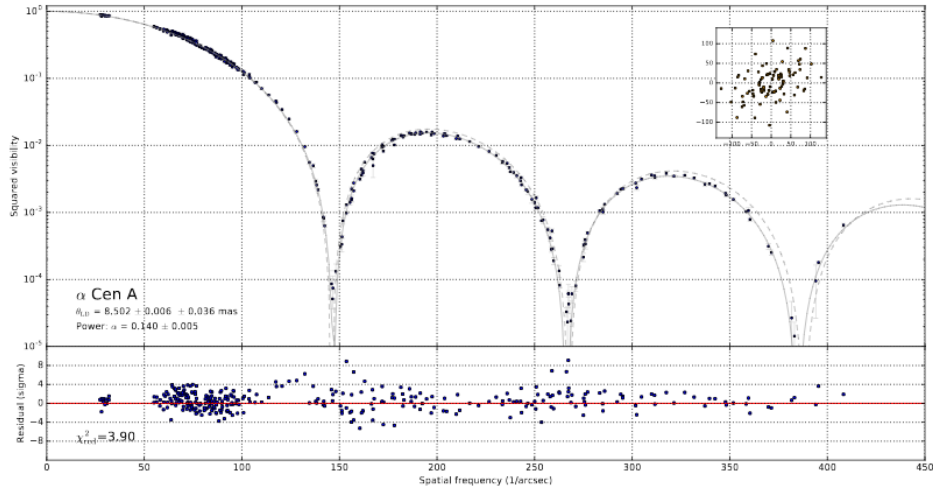


Figure 114. The limb-darkening of α Cen A measured by the Pionier instrument on the VLTI. The dotted line corresponds to a uniform disk model of the star, while the solid line corresponds to a limb-darkened disk model. In paper [69], the authors find a diameter of $\theta_{LD} = 8.502 \pm 0.038$ mas (0.43 % accuracy) using an analytic power law for the limb-darkening, which is then compared to 1D or 3D atmospheric models of limb-darkening.

ments [70, 71]. The agreement is generally good, but gaps are currently observed for giant stars. There is also another way to proceed, without using parallaxes. Asteroseismic scaling relationships [72, 73] rely the mass and radius of the star to the actual temperature, in an independent way. Thus, if one determines the temperature of the star, by spectroscopic measurements for example (historical approach), one obtains the asteroseismic mass and radius. The interferometric diameter can here play an important role, since the temperature can be deduced directly from the bolometric flux of the star and the angular diameter. The problem comes down to compare the temperatures derived by spectroscopy and interferometry, respectively. This is what is currently done on roAp type stars, which have also spots due to their magnetism [74], which are known to alter the derived temperature. Since the roAp have extremely small angular diameters, the VEGA/CHARA instrument, whose spatial resolution is one of the largest in the world (see Figure 104) has been used to measure their angular diameter. For instance, it allowed to measure the angular diameter of 78 Vir and HD24712, which have indeed the smallest diameters ever measured, respectively $\theta_{LD} = 0.346 \pm 0.006$ mas [75] and $\theta_{LD} = 0.335 \pm 0.009$ mas [74] (see Fig. 115).

The determination of the effective temperature of the stars is thus a key issue, which is particularly important when considering metal poor stars. These stars are excellent tracers in galactic archeology, which brings constraints on the structure and evolution of galaxies. As an example, we can mention the star HD140283 observed again with VEGA/CHARA because of its extremely small diameter: $\theta_{LD} = 0.353 \pm 0.013$ mas. These observations were used to compare the spectroscopic (based in particular on the $H\alpha$ spectral line) and interferometric temperatures, while stellar evolution models allow us to deduce the mass and the age of the star. Using a 3D atmosphere model and a CESAM2k stellar evolution model, remarkable accuracies of 1.8% and 7.4% on the mass and age of the star were obtained [76]. Note that this star is particularly interesting because it is part of the 'benchmark' stars of *Gaia*.

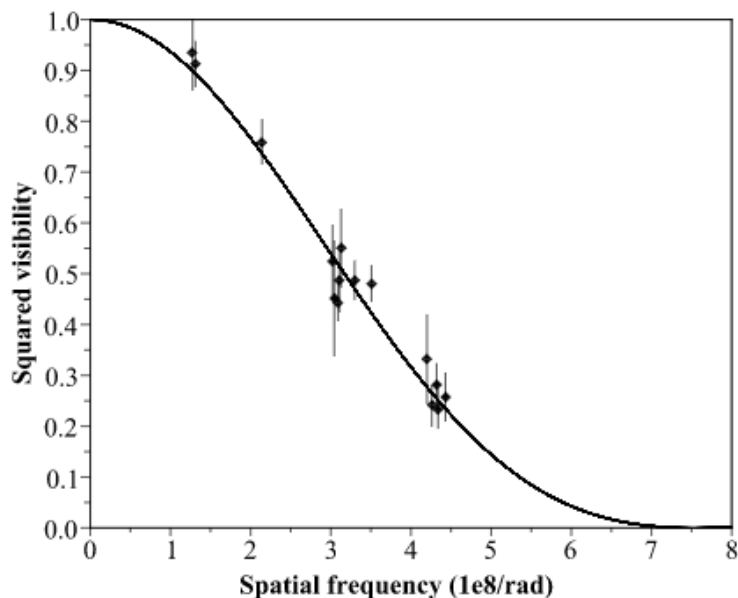


Figure 115. Angular diameter measurement of the roAp 78 Vir done with the VEGA/CHARA instrument. This is one of the smallest angular diameters ever measured, $\theta_{LD} = 0.346 \pm 0.006$ mas [75].

The determination of stellar parameters is an interesting subject in itself, because the stars are the constitutive elements of galaxies, but also because these stellar parameters are indispensable for determining the exo-planetary parameters. Indeed, if we know the ratio of stellar and planetary radii by an exo-planetary transit measurement from space missions, CoRoT, Kepler, K2, TESS or soon PLATO, then *it is enough to know the radius of the star to deduce the radius of the planet*, and therefore its density. Since a 1% accuracy is expected on the transits, an accuracy of 1% on the star radius would be required to deduce the planetary radius at 1%. In this context, the measurements of angular diameters of 10 exoplanet host stars, including one having a transit (55 Cnc), is an important first step to consider [41]. The average accuracy on the derived angular diameters is of about 2% (1.6% for 55 Cnc).

This synergy combining interferometry, asteroseismology, also related to spatial missions *Gaia* and PLATO, is something very interesting that should be followed in the coming decade.

8.6 Doppler Imaging and Hot Jupiter Detection

'Hot Jupiters' orbit on average 100 times closer to their star than Jupiter around the Sun. But how and when in their history do they migrate so close to their star? [77] have just discovered a very young hot Jupiter in the immediate vicinity of a young T Tauri star, barely 2 million years old. But the detection of planets around very young stars proves to be a real challenge, because these stars are very active: their intense magnetic activity disturbs the light emitted by the star significantly. One of the team's prowess was to separate the signal due to the activity of the star from the one generated by the planet. By removing the effect of activity on the ESPaDOnS and Narval velocity curves using Doppler imaging techniques, the team detected a periodic signal of 4.93 ± 0.05 days and a semi-amplitude of 75 ± 11 m/s. This signal completely disconnected from the rotation of the V830 Tau star (2.741 days)

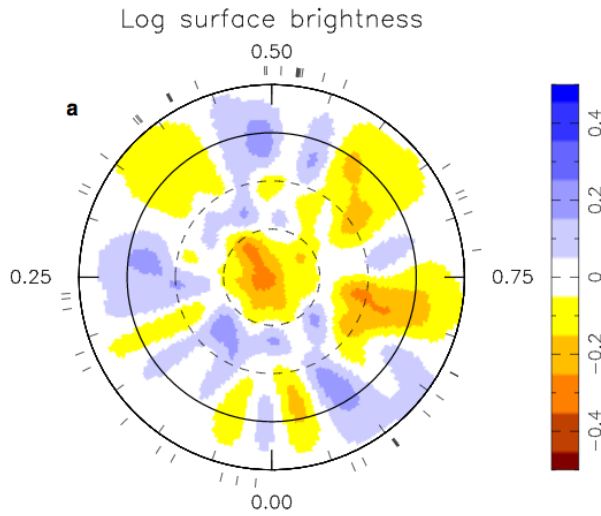


Figure 116. Brightness distribution of the T Tauri V830 Tau obtained from a fit of LSD ('Least Squared Deconvolution' technique) profiles of ESPaDOnS and Narval, according to the Doppler imaging method [77]. The cold and hot spots are represented in brown and blue, respectively.

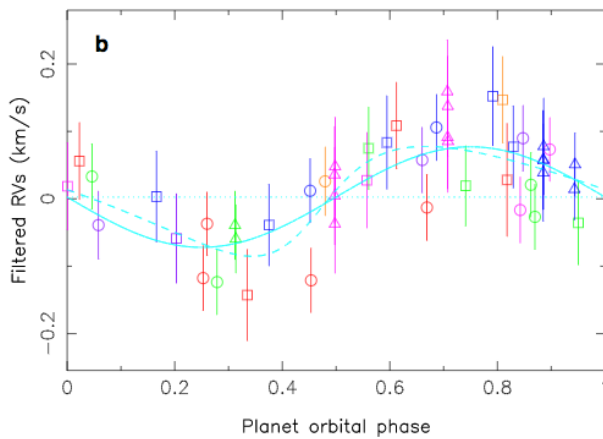


Figure 117. Radial velocity curves of a hot Jupiter around V830 Tau. The Doppler Imaging technique was used to determine the activity of the star, whose velocimetric signature was removed from the ESPaDOnS and Narval observations. The residual radial velocity curve is attributed to the presence of a hot Jupiter [77].

is thus attributed to the presence of a mass planet $0.77 \pm 0.15 M_{\text{J}}$ orbiting at a distance of 0.057 ± 0.001 of the host star. This discovery thus confirms that early migration within the disk is possible in the case of giant planets, the other hypothesis being a migration arriving erratically later in the history of the system by the interplay between planets.

Here we see the power of Doppler imaging, which can be combined (if the object is bright enough) with interferometric measurements as we have already mentioned in the case of red giants and supergiants.

8.7 Detection of the gravitational redshift in the orbit of the star S2 near the Galactic center massive black hole

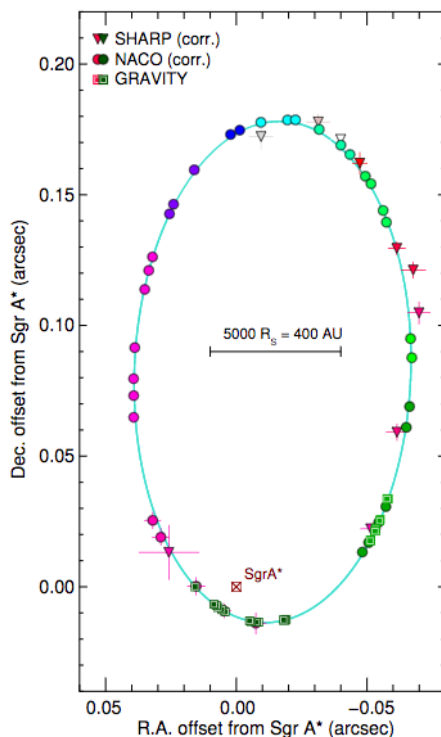


Figure 118. Verification of Einstein's theory of General Relativity near the supermassive black hole (Sgr A*) by the GRAVITY/VLTI instrument.

Before concluding, we would like to emphasize a recent spectacular result obtained by the team in charge of the GRAVITY instrument at the VLTI. By accurately determining the trajectory of the S2 star in orbit around the supermassive black hole located at the center of the Milky Way (Sgr A*), measurements of the GRAVITY instrument (astrometry) made it possible to determine the gravitational redshift of the S2 star and thus confirm the theory of relativity of Einstein [78]. Indeed, at periastron, i.e. at 120 ua of the black hole or 1400 Schwarzschild' radii, the star has an orbital velocity of 7640 km/s, a velocity sufficiently large for the effects of relativity to become measurable (see Fig. 118).

9 Steps to the future

Optical interferometry has made important progresses these last three decades after the pioneering works of the first instruments. It is interesting to compare these progresses with the same ones done in radio-interferometry (see Fig. 119).

If one looks at the progression of the publications in optical interferometry, it can be understood that this domain mimics the radio-interferometry developments with a shift of thirty years in fact!

In the next decade, we can anticipate several synergies:

- direct visible imaging and radio interferometry that allow to superimpose images at different wavelengths but with the same angular resolution (case of the AGB star L2 Pup);
- interferometric and Doppler imaging, which both allow to see the spots on the surface of stars (case of Betelgeuse), as well as Doppler imaging and velocimetry for the detector of exo-Jupiters (case of the Tauri V830 Tau);
- direct imaging and interferometry: for example, detection of exoplanets by imaging with SPHERE and determination of the interferometric diameter of the host star to determine the age of the system (case of GJ504);
- the interferometry in the *continuum* and in a spectral line ($H\alpha$ for example) to probe both the geometry and the kinematics of the studied object (case of the Be star ϕ Per, but also of young stars);
- interferometry and asteroseismology for the determination of stellar and planetary parameters.

Beyond these synergies, the road will continue for sure and we will, in the future, reach facilities with a large number of sub-apertures and an incredible imaging power. An international group is developing the conceptual studies for a project called Planet Finder Imager [79]. However the complexity of such developments because of the current technology and concepts used in the current facilities may prevent the astronomical community to see these facilities operating one day. Other alternatives are considered, such as intensity interferometry or space developments in order to simplify the implementation technology.

We are also developing a demonstrator of a new kind of recombination based on the principle of the Arecibo radio telescope. The idea is to replace the pointing primary mirror (or mirrors in the case of an interferometer) by a fixed primary mirror and a moving gondola acquiring the moving image on the focal sphere. This has proven to be well adapted at radio wavelengths with the long life of the Arecibo radio telescope. The concept has even been improved recently with a continuously deformable primary mirror of 500m in diameter (the FAST Chinese radio telescope [84]) to permanently match the required parabola primary to avoid the limits generated by the spherical aberration of a spherical primary mirror. The very interesting feature of such a configuration is that it permits to avoid the implementation of long delay lines and that it highly simplifies the transfer of beams from the collecting sub apertures to the combiner. We have started the development of a demonstrator [85] in a valley of the Southern Alps, as represented on Fig. 120.

Although the first results of this prototype are highly encouraging in terms of control and accuracy of tracking, the way is still long before a full implementation of a complete system. A space-based or moon-version of such an ambitious hypertelescope is maybe the correct development that will have to be done in the future. However the current facilities like the VLTI or CHARA have still a great potential of developments in the coming decade, with improved adaptive optics systems, fringe sensor, additional telescopes or additional wavebands. And, as said previously, the need for high angular resolution beyond the diffraction limit of single telescopes is clearly the main driver of the future development of this observing technique.

References

- [1] A.A. Michelson, ApJ **51**, 257 (1920)

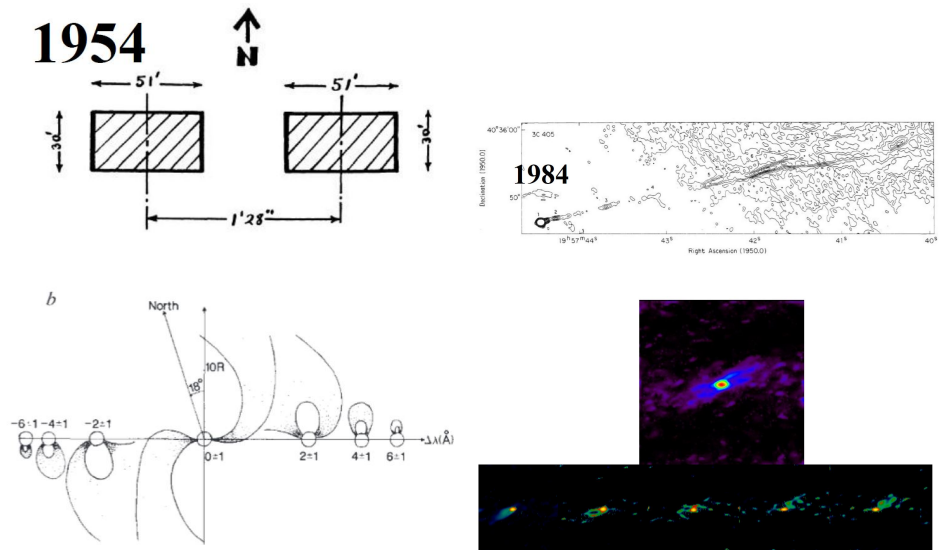


Figure 119. Comparison of the representation of a radio source between 1954 and 1984 (top row: from Jennison [80] and Perley [81]), and in the optical domain between 1989 and 2015 [82, 83]

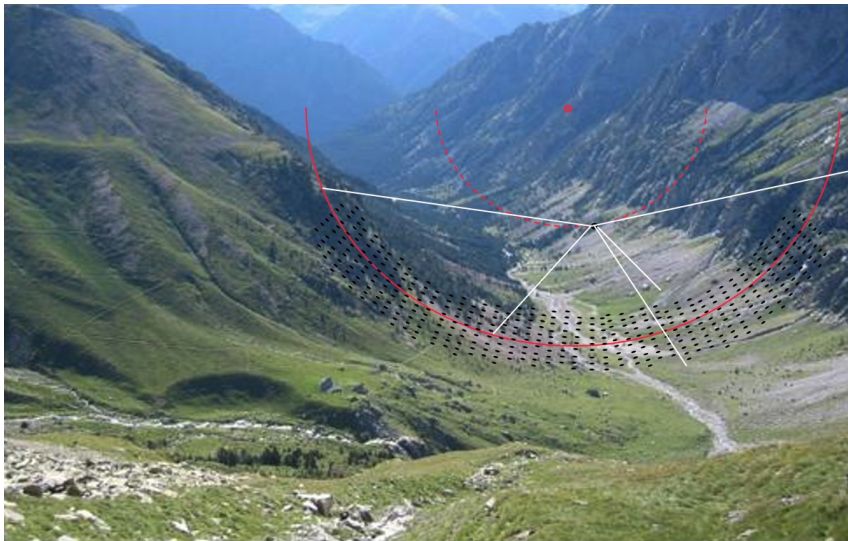


Figure 120. Representation of the installation of the Ubaye Hypertelescope prototype in a valley of the Southern Alps. The primary mirror, made of small segments of 20cm in diameter, is fixed on the ground and matches a large sphere with 202m in radius of curvature. A focal gondola located 101m above the primary mirror is located on the focal sphere and is moved to permanently stay at the location of the moving image of the star.

- [2] H. Fizeau, CRAS (1868)
- [3] A. Labeyrie, ApJ **196**, L71 (1975)
- [4] J.W. Goodman, *Statistical Optics* (1985)
- [5] R.H. Brown, Nature **218**, 637 (1968)
- [6] A. Labeyrie, A&A Sup.Ser. **118**, 517 (1996), astro-ph/9602093
- [7] O. Lardière, F. Martinache, F. Patru, MNRAS **375**, 977 (2007), astro-ph/0612074
- [8] F. Patru, D. Mourard, O. Lardière, S. Lagarde, MNRAS **376**, 1047 (2007), astro-ph/0701467
- [9] A. Labeyrie, D. Mourard, F. Allouche, R. Chakraborty, J. Dejonghe, A. Surya, Y. Bresson, C. Aime, D. Mary, A. Carlotti, *Concept study of an Extremely Large Hyper Telescope (ELHyT) with 1200m sparse aperture for direct imaging at 100 micro-arcsecond resolution*, in *Optical and Infrared Interferometry III* (2012), Vol. 8445, p. 844512
- [10] A. Labeyrie, F. Allouche, D. Mourard, F. Bolgar, R. Chakraborty, J. Maillot, N. Palitzkyne, J.R. Poletti, J.P. Rochaix, R. Prud'homme et al., *Construction of a 57m hyper-telescope in the Southern Alps*, in *Optical and Infrared Interferometry III* (2012), Vol. 8445, p. 844511
- [11] M. Tallon, I. Tallon-Bosc, A&A **253**, 641 (1992)
- [12] P. Berio, D. Mourard, F. Vakili, J. Borgnino, A. Ziad, Journal of the Optical Society of America A **14**, 114 (1997)
- [13] L. Koechlin, P.R. Lawson, D. Mourard, A. Blazit, D. Bonneau, F. Morand, P. Stee, I. Tallon-Bosc, F. Vakili, Applied Optics **35**, 3002 (1996)
- [14] M. Gai, S. Menardi, S. Cesare, B. Bauvir, D. Bonino, L. Corcione, M. Dimmler, G. Massone, F. Reynaud, A. Wallander, *The VLTI fringe sensors: FINITO and PRIMA FSU*, in *New Frontiers in Stellar Interferometry*, edited by W.A. Traub (2004), Vol. 5491 of *Proc. of the SPIE Conference*, p. 528
- [15] Gravity Collaboration, R. Abuter, M. Accardo, A. Amorim, N. Anugu, G. Ávila, N. Azouaoui, M. Benisty, J.P. Berger, N. Blind et al., A&A **602**, A94 (2017), 1705.02345
- [16] D. Mekarnia, J. Gay, Journal of Optics **20**, 131 (1989)
- [17] A.R. Thompson, J.M. Moran, G.W. Swenson, Jr., *Interferometry and Synthesis in Radio Astronomy, 3rd Edition* (2017)
- [18] E.V. Garcia, M.W. Muterspaugh, G. van Belle, J.D. Monnier, K.G. Stassun, A. Ghasempour, J.H. Clark, R.T. Zavala, J.A. Benson, D.J. Hutter et al., PASP **128**, 055004 (2016), 1601.00036
- [19] B. Lazareff, J.B. Le Bouquin, J.P. Berger, A&A **543**, A31 (2012)
- [20] B. Lopez, S. Lagarde, W. Jaffe, R. Petrov, M. Schöller, P. Antonelli, U. Beckmann, P. Berio, F. Bettonvil, A. Glindemann et al., The Messenger **157**, 5 (2014)
- [21] J. Sturmman, T. Ten Brummelaar, L. Sturmman, H.A. McAlister, *Dual three-way infrared beam combiner at the CHARA Array*, in *Society of Photo-Optical Instrumentation Engineers (SPIE) Conference Series* (2010), Vol. 7734 of *Presented at the Society of Photo-Optical Instrumentation Engineers (SPIE) Conference*
- [22] N.J. Scott, R. Millan-Gabet, E. Lhomé, T.A. Ten Brummelaar, V. Coudé Du Foresto, J. Sturmman, L. Sturmman, Journal of Astronomical Instrumentation **2**, 1340005 (2013)
- [23] J.D. Monnier, M. Zhao, E. Pedretti, N. Thureau, M. Ireland, P. Muirhead, J.P. Berger, R. Millan-Gabet, G. Van Belle, T. ten Brummelaar et al., *Imaging the surface of Altair and a MIRC update*, in *Society of Photo-Optical Instrumentation Engineers (SPIE) Conference Series* (2008), Vol. 7013 of *Presented at the Society of Photo-Optical Instrumentation Engineers (SPIE) Conference*

- [24] M.J. Ireland, A. Mérand, T.A. ten Brummelaar, P.G. Tuthill, G.H. Schaefer, N.H. Turner, J. Sturmman, L. Sturmman, H.A. McAlister, *Sensitive visible interferometry with PAVO*, in *Society of Photo-Optical Instrumentation Engineers (SPIE) Conference Series* (2008), Vol. 7013 of *Presented at the Society of Photo-Optical Instrumentation Engineers (SPIE) Conference*
- [25] D. Mourard, J.M. Clausse, A. Marcotto, K. Perraut, I. Tallon-Bosc, P. Bériot, A. Blazit, D. Bonneau, S. Bosio, Y. Bresson et al., *A&A* **508**, 1073 (2009)
- [26] D. Mourard, P. Bériot, K. Perraut, R. Ligi, A. Blazit, J.M. Clausse, N. Nardetto, A. Spang, I. Tallon-Bosc, D. Bonneau et al., *A&A* **531**, A110 (2011)
- [27] A. Labeyrie, *Exo-Earth Imager for Exoplanet Snapshots with Resolved Detail*, in *Working on the Fringe: Optical and IR Interferometry from Ground and Space*, edited by S. Unwin, R. Stachnik (1999), Vol. 194 of *Astronomical Society of the Pacific Conference Series*, p. 350
- [28] C. Paladini, F. Baron, A. Jorissen, J.B. Le Bouquin, B. Freytag, S. van Eck, M. Witkowski, J. Hron, A. Chiavassa, J.P. Berger et al., *Nature* **553**, 310 (2018)
- [29] M. Montargès, P. Kervella, G. Perrin, A. Chiavassa, J.B. Le Bouquin, M. Aurière, A. López Ariste, P. Mathias, S.T. Ridgway, S. Lacour et al., *A&A* **588**, A130 (2016), 1602.05108
- [30] M. Montargès, A. Chiavassa, P. Kervella, S.T. Ridgway, G. Perrin, J.B. Le Bouquin, S. Lacour, *A&A* **605**, A108 (2017), 1705.07829
- [31] A. Chiavassa, R. Norris, M. Montargès, R. Ligi, L. Fossati, L. Bigot, F. Baron, P. Kervella, J.D. Monnier, D. Mourard et al., *A&A* **600**, L2 (2017), 1703.02406
- [32] R.M. Roettenbacher, J.D. Monnier, H. Korhonen, A.N. Aarnio, F. Baron, X. Che, R.O. Harmon, Z. Kővári, S. Kraus, G.H. Schaefer et al., *Nature* **533**, 217 (2016), 1709.10107
- [33] B. Freytag, S. Liljegren, S. Höfner, *A&A* **600**, A137 (2017), 1702.05433
- [34] M. Aurière, A. López Ariste, P. Mathias, A. Lèbre, E. Josselin, M. Montargès, P. Petit, A. Chiavassa, F. Paletou, N. Fabas et al., *A&A* **591**, A119 (2016), 1605.04702
- [35] B. Tessore, A. Lèbre, J. Morin, P. Mathias, E. Josselin, M. Aurière, *A&A* **603**, A129 (2017), 1704.07761
- [36] A. Lèbre, M. Aurière, N. Fabas, D. Gillet, F. Herpin, R. Konstantinova-Antova, P. Petit, *A&A* **561**, A85 (2014), 1310.4379
- [37] D. Mourard, J.M. Clausse, A. Marcotto, K. Perraut, I. Tallon-Bosc, P. Bériot, A. Blazit, D. Bonneau, S. Bosio, Y. Bresson et al., *A&A* **508**, 1073 (2009)
- [38] P. Kervella, M. Montargès, E. Lagadec, S.T. Ridgway, X. Haubois, J.H. Girard, K. Ohnaka, G. Perrin, A. Gallenne, *A&A* **578**, A77 (2015), 1511.04448
- [39] P. Kervella, W. Homan, A.M.S. Richards, L. Decin, I. McDonald, M. Montargès, K. Ohnaka, *A&A* **596**, A92 (2016), 1611.06231
- [40] M. Bonnefoy, K. Perraut, A.M. Lagrange, P. Delorme, A. Vigan, M. Line, L. Rodet, C. Ginski, D. Mourard, G.D. Marleau et al., *ArXiv e-prints* (2018), 1807.00657
- [41] R. Ligi, O. Creevey, D. Mourard, A. Crida, A.M. Lagrange, N. Nardetto, K. Perraut, M. Schultheis, I. Tallon-Bosc, T. ten Brummelaar, *A&A* **586**, A94 (2016), 1511.03197
- [42] G. Dalla Vedova, F. Millour, A. Domiciano de Souza, R.G. Petrov, D. Moser Faes, A.C. Carciofi, P. Kervella, T. Rivinius, *A&A* **601**, A118 (2017), 1703.02839
- [43] D. Mourard, J.D. Monnier, A. Meilland, D. Gies, F. Millour, M. Benisty, X. Che, E.D. Grundstrom, R. Ligi, G. Schaefer et al., *A&A* **577**, A51 (2015), 1503.03423
- [44] A. Domiciano de Souza, P. Kervella, D. Moser Faes, G. Dalla Vedova, A. Mérand, J.B. Le Bouquin, F. Espinosa Lara, M. Rieutord, P. Bendjoya, A.C. Carciofi et al., *A&A* **569**,

- A10 (2014)
- [45] M. Challouf, N. Nardetto, A. Domiciano de Souza, D. Mourard, H. Aroui, P. Stee, O. Delaa, D. Graczyk, G. Pietrzyński, W. Gieren, *A&A* **579**, A107 (2015)
- [46] A. Mérand, P. Kervella, J. Breitsfelder, A. Gallenne, V. Coudé du Foresto, T.A. ten Brummelaar, H.A. McAlister, S. Ridgway, L. Sturmann, J. Sturmann et al., *A&A* **584**, A80 (2015), 1510.01940
- [47] G. Pietrzyński, D. Graczyk, W. Gieren, I.B. Thompson, B. Pilecki, A. Udalski, I. Soszyński, S. Kozłowski, P. Konorski, K. Suchomska et al., *Nature* **495**, 76 (2013), 1303.2063
- [48] D. Graczyk, P.F.L. Maxted, G. Pietrzyński, B. Pilecki, P. Konorski, W. Gieren, J. Storm, A. Gallenne, R.I. Anderson, K. Suchomska et al., *A&A* **581**, A106 (2015), 1508.03188
- [49] A. Gallenne, G. Pietrzyński, D. Graczyk, N. Nardetto, A. Mérand, P. Kervella, W. Gieren, S. Villanova, R.E. Mennickent, B. Pilecki, *ArXiv e-prints* (2018), 1806.09572
- [50] A. Gallenne, P. Kervella, A. Mérand, G. Pietrzyński, W. Gieren, N. Nardetto, B. Trahin, *A&A* **608**, A18 (2017), 1708.09851
- [51] N. Nardetto, E. Poretti, M. Rainer, A. Fokin, P. Mathias, R.I. Anderson, A. Gallenne, W. Gieren, D. Graczyk, P. Kervella et al., *A&A* **597**, A73 (2017), 1701.01589
- [52] P. Kervella, W. Homan, A.M.S. Richards, L. Decin, I. McDonald, M. Montargès, K. Ohnaka, *A&A* **596**, A92 (2016), 1611.06231
- [53] N. Nardetto, A. Mérand, D. Mourard, J. Storm, W. Gieren, P. Fouqué, A. Gallenne, D. Graczyk, P. Kervella, H. Neilson et al., *A&A* **593**, A45 (2016), 1609.07268
- [54] M. Benisty, A. Juhasz, A. Boccaletti, H. Avenhaus, J. Milli, C. Thalmann, C. Dominik, P. Pinilla, E. Buenzli, A. Pohl et al., *A&A* **578**, L6 (2015), 1505.05325
- [55] A. Garufi, S.P. Quanz, H.M. Schmid, G.D. Mulders, H. Avenhaus, A. Boccaletti, C. Ginski, M. Langlois, T. Stolker, J.C. Augereau et al., *A&A* **588**, A8 (2016), 1601.04983
- [56] G.A. Muro-Arena, C. Dominik, L.B.F.M. Waters, M. Min, L. Klarmann, C. Ginski, A. Isella, M. Benisty, A. Pohl, A. Garufi et al., *A&A* **614**, A24 (2018), 1802.03328
- [57] K. Rousset-Perraut, M. Benisty, D. Mourard, S. Rajabi, F. Bacciotti, P. Bériot, D. Bonneau, O. Chesneau, J.M. Clausse, O. Delaa et al., *A&A* **516**, L1 (2010), 1005.5267
- [58] L.E. Ellerbroek, M. Benisty, S. Kraus, K. Perraut, J. Kluska, J.B. le Bouquin, M. Borges Fernandes, A. Domiciano de Souza, K.M. Maaskant, L. Kaper et al., *A&A* **573**, A77 (2015), 1409.7394
- [59] Gravity Collaboration, R. Abuter, M. Accardo, A. Amorim, N. Anugu, G. Ávila, N. Azouaoui, M. Benisty, J.P. Berger, N. Blind et al., *A&A* **602**, A94 (2017), 1705.02345
- [60] Gravity Collaboration, R. Garcia Lopez, K. Perraut, A. Caratti O Garatti, B. Lazareff, J. Sanchez-Bermudez, M. Benisty, C. Dougados, L. Labadie, W. Brandner et al., *A&A* **608**, A78 (2017)
- [61] F. Anthonioz, F. Ménard, C. Pinte, J.B. Le Bouquin, M. Benisty, W.F. Thi, O. Absil, G. Duchêne, J.C. Augereau, J.P. Berger et al., *A&A* **574**, A41 (2015), 1412.1052
- [62] C. Thalmann, G.D. Mulders, M. Janson, J. Olofsson, M. Benisty, H. Avenhaus, S.P. Quanz, H.M. Schmid, T. Henning, E. Buenzli et al., *ApJ Letters* **808**, L41 (2015), 1507.03587
- [63] D. Mourard, M. Broz, J. Nemravova, P. Harmanec, J. Budaj, F. Baron, J. Monnier, G. Schaefer, H. Schmitt, I. Tallon-Bosc et al., *ArXiv e-prints* (2018), 1807.04789
- [64] A. Chelli, G. Duvert, L. Bourguès, G. Mella, S. Lafrasse, D. Bonneau, O. Chesneau, *A&A* **589**, A112 (2016), 1604.07700

- [65] M. Challouf, N. Nardetto, D. Mourard, D. Graczyk, H. Aroui, O. Chesneau, O. Delaa, G. Pietrzyński, W. Gieren, R. Ligi et al., *A&A* **570**, A104 (2014), 1409.1351
- [66] L. Bigot, D. Mourard, P. Berio, F. Thévenin, R. Ligi, I. Tallon-Bosc, O. Chesneau, O. Delaa, N. Nardetto, K. Perraut et al., *A&A* **534**, L3 (2011), 1110.0985
- [67] Z. Magic, A. Chiavassa, R. Collet, M. Asplund, *A&A* **573**, A90 (2015), 1403.3487
- [68] A. Chiavassa, A. Caldas, F. Selsis, J. Leconte, P. Von Paris, P. Bordé, Z. Magic, R. Collet, M. Asplund, *A&A* **597**, A94 (2017), 1609.08966
- [69] P. Kervella, L. Bigot, A. Gallenne, F. Thévenin, *A&A* **597**, A137 (2017), 1610.06185
- [70] D. Huber, M.J. Ireland, T.R. Bedding, I.M. Brandão, L. Piau, V. Maestro, T.R. White, H. Bruntt, L. Casagrande, J. Molenda-Żakowicz et al., *ApJ* **760**, 32 (2012), 1210.0012
- [71] E.K. Baines, J.T. Armstrong, H.R. Schmitt, J.A. Benson, R.T. Zavala, G.T. van Belle, *ApJ* **781**, 90 (2014), 1401.3342
- [72] Y. Lebreton, M.J. Goupil, J. Montalbán, *How accurate are stellar ages based on stellar models?. II. The impact of asteroseismology*, in *EAS Publications Series* (2014), Vol. 65 of *EAS Publications Series*, pp. 177–223, 1410.5337
- [73] B. Mosser, *Stellar oscillations - I - The adiabatic case*, in *EAS Publications Series* (2015), Vol. 73 of *EAS Publications Series*, pp. 3–110, 1509.08077
- [74] K. Perraut, I. Brandão, M. Cunha, D. Shulyak, D. Mourard, N. Nardetto, T.A. ten Brummelaar, *A&A* **590**, A117 (2016)
- [75] K. Perraut, M. Cunha, I. Brandão, J. Loredat, D. Mourard, A. Meilland, N. Nardetto, H. McAlister, T.A. ten Brummelaar, J. Sturmann et al., *A&A* **579**, A85 (2015)
- [76] O.L. Creevey, F. Thévenin, P. Berio, U. Heiter, K. von Braun, D. Mourard, L. Bigot, T.S. Boyajian, P. Kervella, P. Morel et al., *A&A* **575**, A26 (2015), 1410.4780
- [77] J.F. Donati, C. Moutou, L. Malo, C. Baruteau, L. Yu, E. Hébrard, G. Hussain, S. Alencar, F. Ménard, J. Bouvier et al., *Nature* **534**, 662 (2016), 1606.06236
- [78] Gravity Collaboration, R. Abuter, A. Amorim, N. Anugu, M. Bauböck, M. Benisty, J.P. Berger, N. Blind, H. Bonnet, W. Brandner et al., *A&A* **615**, L15 (2018), 1807.09409
- [79] J.D. Monnier, S. Kraus, M.J. Ireland, F. Baron, A. Bayo, J.P. Berger, M. Creech-Eakman, R. Dong, G. Duchêne, C. Espillat et al., *Experimental Astronomy* (2018)
- [80] R.C. Jennison, M.K. Das Gupta, *Nature* **172**, 996 (1953)
- [81] R.A. Perley, J.W. Dreher, J.J. Cowan, *ApJ Letters* **285**, L35 (1984)
- [82] D. Mourard, I. Bosc, A. Labeyrie, L. Koechlin, S. Saha, *Nature* **342**, 520 (1989)
- [83] D. Mourard, J.D. Monnier, A. Meilland, D. Gies, F. Millour, M. Benisty, X. Che, E.D. Grundstrom, R. Ligi, G. Schaefer et al., *A&A* **577**, A51 (2015), 1503.03423
- [84] R. Nan, *Introduction to FAST: five hundred meter Aperture Spherical radio Telescope*, in *Ground-based and Airborne Telescopes II* (2008), Vol. 7012, p. 70121E
- [85] D. Mourard, A. Labeyrie, T. Lepine, P.D. Nunez, B. Tregon, Z. Xie, *Experimental Astronomy* (2018)